Fuel 377 (2024) 132817

Contents lists available at ScienceDirect

Fuel

journal homepage: www.elsevier.com/locate/fuel

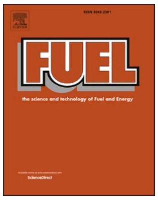

Full Length Article

Computational simulation of SE-SR of methane in a bench-scale circulating fluidised bed reactor: Insights into the effects of bed geometry design and catalyst-sorbent ratios

Chinonyelum Udemu, Carolina Font-Palma *

School of Engineering, University of Hull, Hull HU6 7RX, UK

ARTICLE INFO

Keywords:
SE-SMR
Hydrogen
CCS
CPFD

ABSTRACT

Operating sorbent-enhanced steam reforming (SE-SR) of methane in fluidised bed reactors presents a promising pathway for industrial low-carbon hydrogen production. However, further understanding of its complex multiphase behaviours under certain operating conditions is still needed to guide reactor design and scale-up. This study developed a computational particle fluid dynamic (CPFD) reactor model to study cyclic SE-SR performance. The model was used to simulate scenarios representing potential reductions in catalyst activity and sorbent inventory levels over time by varying catalyst-sorbent ratios. Additionally, the effects of two different bed geometry designs were examined.

Results indicate that varying solids ratios influenced reaction progress, with optimised methane conversion and CO_2 capture observed at moderate ratios. Higher sorbent loadings enhanced thermal neutrality but risked increased calciner energy penalties. Bed geometry also influenced localised hydrodynamics. Detailed solids and gas concentration contours provided insight into segregation and spatial product distribution in the two designs.

1. Introduction

Hydrogen has a high energy density by mass and produces only water vapor when combusted or used in a fuel cell, making it an attractive alternative to fossil fuels from a sustainability and emissions standpoint [1]. However, current methods of large scale hydrogen production like steam reforming and gasification are fossil fuel-based with huge CO_2 emissions, and significant infrastructure would need to be built to produce cleaner hydrogen at scale. While electrolysis and other renewable hydrogen production methods are important long-term solutions, carbon capture and storage (CCS) can play a key role in the transition away from conventional fossil fuel-based hydrogen production. Steam reforming with integrated CCS like sorption-enhanced steam reforming (SE-SR) technology offers advantages as an intermediate option. In SE-SR, a physical sorbent material like calcium oxide is integrated directly into the steam reforming reactor to capture and remove CO_2 from the reforming process as it occurs, allowing for an overall capture efficiency of ~99 % and lowering CO_2 emissions per unit of hydrogen produced [2]. The overall SE-SR process involves two key reactions: the steam reforming reaction that produces hydrogen represented by Eq. (1), and the carbonation/regeneration reaction in which the sorbent material captures CO_2 and is regenerated, as shown in Eq. (2). M in Eq. (2) represents the sorbent, usually alkaline-earth or alkali-based metals.

$$C_aH_bO_c + (2a-c)H_2O \rightleftharpoons \left(2a-c+\frac{1}{2}b\right)H_2 + aCO_2 \tag{1}$$

$$MO_{a(s)} + CO_{2(g)} \rightleftharpoons MCO_{3(s)} \tag{2}$$

Large-scale production of hydrogen via SE-SR of methane requires continuous operation of the process and solids circulation between the reformer/carbonator and calciner. Various reactor concepts have been proposed and reported for SE-SR of methane, including trickle bed, packed bed and fluidised bed reactors. In trickle bed, the gaseous reactants are passed from the bottom through an immobilised bed of catalysts while the sorbents are introduced into the reactor from the top, and collected at the bottom [3,4]. Formation of hotspots within the catalysts and scaleup challenges due to its complex phenomena are setbacks associated with this reactor concept [5,6]. For packed bed reactors, a fixed ratio of sorbents and catalyst is contained in a reactor, with gaseous reactants passed over the bed of mixed solids to produce hydrogen [7,8]. Whilst fixed-bed reactors are simpler and are well-

---

* Corresponding author.
E-mail address: C.Font-Palma@hull.ac.uk (C. Font-Palma).

https://doi.org/10.1016/j.fuel.2024.132817
Received 29 February 2024; Received in revised form 31 July 2024; Accepted 14 August 2024

Nomenclature

CCE	CO_2 capture efficiency
CCS	Carbon capture and storage
CFB	Circulating fluidised bed
CPFD	Computational particle fluid dynamics
C-S	Catalyst-to-sorbent ratio
EMMS	Energy minimization multiscale
LHV	Low heating value
MP-PIC	Multiphase particle-in-cell
PE	Process efficiency
S/C	Steam-to-carbon ratio
SE-SMR	Sorption-enhanced steam methane reforming
SE-SR	Sorption-enhanced steam reforming
SMR	Steam methane reforming
WGS	Water-gas shift
D_p	Drag function, [kg/m^3 s]
D_t	Turbulent mass diffusivity, [m^2/s]
E_a	Activation energy, [kJ/mol]
F	Interface momentum transfer between the particle and gas phase, [N/m^3 s]
h_{fw}, h_l, h_d	Fluid-to-wall, lean gas, dense particle heat transfer coefficient, [W/(m^{2}K)]
K_{SMR}, K_{WGS}	Equilibrium constant of SMR, WGS reactions, [atm^2], [-]
k_{ad}	Adsorption constant, [atm^{-2}]
k_g	Thermal conductivity of the gas (Table 2), [W/(mK)]
k^0_{SMR}	Rate constant for SMR in NK model, [kmol/(kg s atm$^{0.404}$)]
k^0_{WGS}	Rate constant for WGS in NK model, [kmol/(kg s atm)]
m	Mass flow rate, [kg/s]
M	Molecular weight, [kg mol^{-1}]
n	Parameter in the sorption rate equation
p	Partial pressure, [atm]
P	Total pressure, [atm]
Pr	Prandtl number, [-]
q	Heat flux [W/m^2]
$\dot{q}_d$	Enthalpy diffusion term [J/(m^3 s)]
R	Rate of reaction, [kmol/ kg$^{-1}_{cat}$s^{-1}]
Re	Reynolds number, [-]
S	Sorbent's specific surface area, [m^2/kg]
S_h	Energy exchange between the particle and the gas phase, [J/(m^3 s)]
S_i	Interpolation operator for node i
T	Temperature, [K]
u	Velocity, [m/s]
x	Molar flow rate, [mol/s]
X	Conversion, [%]
Y_{H_2}	Hydrogen yield, [%]
Greek	
ρ	Density [kg/m^3]
Ï	Volume fraction [-]
τ	Stress tensor, [Pa]
µ	Viscosity, [Pas]
ε	Constant parameter in equation (10)
ξ	Face node
Subscripts	
cp	Close-pack
fw	Fluid-to-wall
g	Gas
p	Particle

suited for high-pressure hydrogen production, they could face challenges with temperature control (to prevent the formation of hotspots) at large-scale operation [9]. Also, solids circulation between reforming/carbonation and calcination reactors can be complicated using this reactor concept. Thus, fluidised bed reactors were selected for this study due to their suitability for facilitating the continuous circulation of solids between reactors, a key requirement for the sorption-enhanced steam reforming process. This continuous circulation loop is integral to maintaining the sorbent circulation necessary for hydrogen production on an industrial scale.

Few configurations of fluidised bed reactors have been proposed for use in SE-SR of methane, such as the use of dual bubbling fluidised bed reactors for both the reformer and calciner units [10,11], the employment of fast fluidised bed (risers) and bubbling bed reactors for the calciner and reformer, respectively [12–14], and the use of fast fluidised for both reformer and calciner [15]. However, riser reformers have been shown to achieve lower hydrogen yields than bubbling bed reformers due to the shorter solids' residence time in the reactor. Jakobsen and Halmøy's [16] modelling study provided a valuable comparison of performance between SE-SR using bubbling and riser fluidised beds reformers with lithium orthosilicate, sodium zirconate, and dolomite sorbents. In their study, using CaO as the sorbent in a riser reactor resulted in only a modest increase in hydrogen yield due to slow sorption kinetics and insufficient solids residence time for CaO to achieve significant conversion. This meant that an exceptionally long riser would be needed to adequately enhance the reforming process via sorption. In contrast, bubbling bed simulations showed much higher hydrogen yields of up to 99.9 %. Whilst a bubbling fluidised bed configuration is preferable to a riser for SE-SR of methane with CaO due to residence time considerations, the reactor geometry and design could impact process performance. Features like aspect ratio, inlet/outlet positioning and internals can influence solids mixing and stratification, respectively enhancing or hindering mass transfer between phases [17–20].

Previous studies have investigated the impacts of key operating variables like temperature, pressure and gas velocity on SE-SR of methane [21]; however, the influence of the catalyst-to-sorbent ratio and reactor design has been relatively underexplored. This work seeks to address this gap by modelling and analysing SE-SR performance under varying solids loadings, in addition to exploring two different dual bubbling circulating fluidised bed (CFB) reactor geometries. Simulations were conducted by intentionally using low catalyst loadings, to provide insights into process behaviour when catalyst activity declines, analogous to real-world catalyst deactivation. Furthermore, testing low sorbent loadings will demonstrate the impact of declining sorbent inventory on the SE-SR of methane performance, similar to sorbent degradation over repeated cycles. Computational particle fluid dynamics (CPFD) software was used to conduct three-dimensional simulations, based on solving continuum equations for the fluid phase coupled with Lagrangian tracking of discrete particles. Constrained by high computational requirements, this study considered only two reactor bed designs as a precursor to our forthcoming work that will scale up the SE-SR system using a simplified configuration (see Fig. 1b) rather than the more complex original experimental setup (see Fig. 1a), whose operational data was instrumental in validating the CPFD model used in this study.

2. Methodology

A CPFD model for SE-SR of methane was developed using Barracuda Virtual Reactor® v23.0.1 software – a specialised fluidised bed reactor

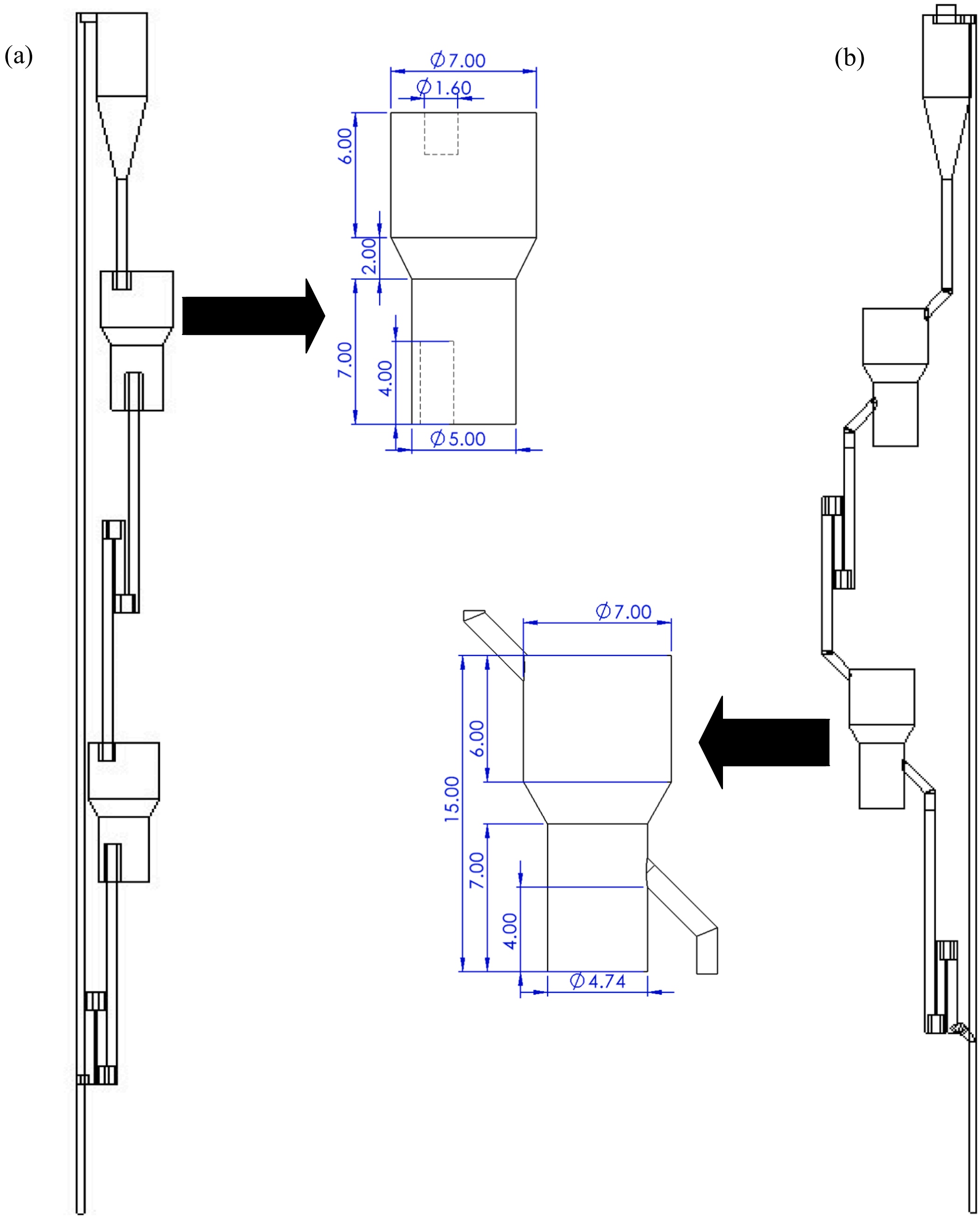

Fig. 1. Design and dimensions of (a) reactor bed design with internal particle outflow (CFB1), and (b) reactor bed design with side particle outflow (CFB2) of the SE-SR reactors used in the simulation.

software. The CPFD model draws on the multiphase particle-in-cell (MP-PIC) approach to resolve the catalyst and sorbent particles as discrete elements, and has been employed to study the kinetic and hydrodynamic interactions in fluidised bed reactors for other chemical processes such as biomass gasification [22,23]. Certain drawbacks observed in modelling approaches like the Eulerian-Eulerian multi-fluid model, such as the inability to fully capture particle-scale interactions for highly-dense beds, can easily be resolved using the CPFD model. Three-dimensional simulations of the SE-SR systems were performed on the University of Hull's high performance computing (HPC) cluster, Viper. Viper is equipped with a large array of powerful graphical processing units (GPUs) and central processing units (CPUs), that allows for computationally-demanding simulations.

2.1. *Reactor setup*

This study models the cyclic performance of SE-SR of methane based on a bench-scale setup similar to that developed at SINTEF [24]. Two reactor systems are evaluated in this study. The first design (Fig. 1a) replicates the system used at SINTEF, and employs a bubbling fluidised bed reactor with an internal pipe for particle outlet from the bottom of the bed. The second design (Fig. 1b) incorporates a side-exit particle outflow mechanism to let out solids from the bed. Both designs consist of interconnected bubbling fluidised bed reactors performing key roles – a reformer/carbonator for the endothermic reforming and exothermic sorption reactions, a calciner for the endothermic calcination reaction, and auxiliary components like loop seals and a riser facilitating

Table 1
Gas flows in the SE-SR system.

Units	Fluidising gas	Superficial velocity (m/s)
Reformer	Nitrogen, steam and methane	0.062
Calciner	Nitrogen	0.056

continuous solids circulation. The internal dimensions of the reactor units are provided in Fig. 1. For each CFB system – CFB1 and CFB2, the reformer/carbonator and calciner have the same dimensions. The bed height and volume are also considered to be constant for CFB1 and CFB2, at the bed volumes considered in this study (see Table 7).

During operation, fluidising gases are introduced to the bottom of the reformer (located just below the cyclone), where reforming and carbonation reactions occur. The product gases leave the reactor from the top while the spent solids leave the reactor through the overflow pipe located inside the reactor for CFB1, and the side exit for CFB2. The solids enter the first loop seal, as seen in Fig. 1, then to the regenerator (second reactor at the bottom). The loop seal is aerated with a fluidising gas, forcing the solids to overflow into the regenerator. The loop seal is attached to maintain the pressure levels, improve solids circulation rate and minimise gas leakages between the reactors. In the regenerator, the hot fluidising gas provides enough heat for decarbonation of the spent sorbent; and operates in similar bubbling manner as the reformer. The regenerated solids overflow to the bottom loop seal and are transported through the riser back to the reformer, using a fluidising gas. The cyclone in this system is only used to return solid particles to the reformer. Completely mixed sorbents and catalysts were introduced into the reactor, with an estimated sorbent-to-catalyst volume ratio of 4 in the reformer. The superficial velocities of the fluidising gases are presented in Table 1.

2.2. Mathematical models

2.2.1. Hydrodynamic and heat transfer model

In the MP-PIC approach, the computational domain is divided into a finite number of Eulerian cells to form a fixed mesh. The fluid phase variables, such as density, velocity and pressure, are defined on this stationary mesh. The particulate phase is modelled using computational particles that are free to move within the domain. Each particle represents a collection of physical particles and tracks their properties in a Lagrangian framework. As the particles traverse the cells over time, their properties are interpolated from the particle locations onto the stationary Eulerian mesh, using an interpolation operator. Likewise, the fluid phase variables defined on the fixed grid, such as hydrodynamic forces – pressure and drag, are interpolated back to the particle positions to update their motion. This coupling between the discrete Lagrangian particle phase and continuous Eulerian fluid phase facilitates multiphase interactions while reducing the computational cost, compared to fully resolving each individual physical particle.

The governing multiphase equations incorporate the conservation of mass, momentum and energy for both phases. Constitutive models describe stress and viscosity relationships. Additional terms account for the exchange of properties between phases via interpolation, as well as interphase forces like gas–solid drag. Together, these equations provide a numerical framework to simulate multiphase flow dynamics efficiently in Barracuda VR® [25].

i. Gas phase

The mass, momentum and energy conservation equations for the gas phase, assuming incompressible fluid phase, are expressed in Eqs. (3)–(5), respectively [26,27].

$$\frac{\partial(\theta_g\rho_g)}{\partial t}+\nabla\hat{A}\cdot(\theta_g\rho_g\boldsymbol{u}_g)=0 \tag{3}$$

$$\frac{\partial(\theta_g\rho_g\boldsymbol{u}_g)}{\partial t}+\nabla\hat{A}\cdot(\theta_g\rho_g\boldsymbol{u}_g\boldsymbol{u}_g)=-\nabla p+\boldsymbol{F}+\theta_g\rho_g\boldsymbol{g}+\nabla\hat{A}\cdot(\theta_g\tau_g) \tag{4}$$

$$\frac{\partial(\theta_g\rho_g h_g)}{\partial t}+\nabla\hat{A}\cdot(\theta_g\rho_g h_g\boldsymbol{u}_g)=\theta_g\left(\frac{\partial p}{\partial t}+\boldsymbol{u}_g\hat{A}\cdot\nabla p\right)-\nabla\hat{A}\cdot(\theta_g\boldsymbol{q})+S_h+\dot{q}_D \tag{5}$$

where $\theta_g, \rho_g, \boldsymbol{u}_g, h_g$, and τ_g are the gas volume fraction, density, velocity, enthalpy, and stress tensor, respectively, for the gas phase. $\boldsymbol{F}$ is the interface momentum transfer and couples the gas phase momentum with the particle motion. The stress tensor is given as:

$$\tau_g=\tau_{g,ij}=\mu_g\left(\frac{\partial u_i}{\partial x_j}+\frac{\partial u_j}{\partial x_i}\right)-\frac{2}{3}\mu_g\delta_{ij}\frac{\partial u_k}{\partial x_k} \tag{6}$$

In addition, the species continuity equations shown in Eq. (7) are solved to determine the mass fraction, $Y_{g,i}$, for each individual gas species, i, present in the multiphase mixture. The species continuity equations describe the conservation of mass for each gas component at every point in space and time. By finding the localised mass fractions, $Y_{g,i}$, the composition of the gas mixture is known at any given location.

$$\frac{\partial(\theta_g\rho_g Y_{g,i})}{\partial t}+\nabla(\theta_g\rho_g Y_{g,i}u_g)=\nabla(\rho_g D_t\theta_g\nabla Y_{g,i})+\delta\dot{m}_{i,chem} \tag{7}$$

The term D_t in the species transport equation represents the turbulent mass diffusivity, which accounts for turbulent mixing effects, while $\delta\dot{m}_{i,chem}$ is the species source term due to chemical reactions occurring in the system.

ii. Particle phase

The particulate phase is defined by the particle distribution function (PDF). The PDF, denoted as ϕ, provides a statistical representation of the particulate phase. It depends on particle properties such as position x, time t, velocity $\boldsymbol{u}_p$, and density ρ_g. To analyse the time evolution of the particulate phase distribution, the Liouville equation is commonly solved. Eq. (8) governs the time evolution of the PDF.

$$\frac{\partial\phi}{\partial t}+\nabla\hat{A}\cdot(\phi\boldsymbol{u}_p)+\nabla_{u_p}\hat{A}\cdot(\phi\boldsymbol{a}_p)=0. \tag{8}$$

The Liouville equation accounts for changes in the PDF due to particle motion via $\boldsymbol{u}_p$, as well as acceleration of particles, $\boldsymbol{a}_p$, via external forces acting on each particle, such as fluid drag and pressure gradient forces. Integration of the PDF over all particle properties yields locally averaged particulate quantities, such as the number density and velocity. Solving the equation also advances the statistical description of the dispersed particle phase in a manner coupled to the fluid phase, defined on the grid.

iii. Gas-particle interphase coupling

In multiphase simulations, modelling the interaction between the dispersed particulate phase and the continuous carrier fluid is essential. This interaction is represented through coupling terms that account for momentum transfer in both directions. These two coupling terms are important for consistent two-way momentum exchange between the gas and solid phases.

Firstly, the particle acceleration ($\boldsymbol{a}_p$) depends on the forces exerted by the surrounding gas on the particles as they move through the flow. This particle acceleration term couples the particle phase to the gas phase in the particle motion equations. This also accounts for drag and other factors that make the particulate motion deviate from pure inertia. The particle acceleration in the Liouville equation is expressed as [26]:

$$\boldsymbol{a}_p = D_p\left(\boldsymbol{u}_g - \boldsymbol{u}_p\right) - \frac{1}{\rho_p}\nabla p + \boldsymbol{g} - \frac{1}{\theta_p\rho_p}\nabla\tau_p \tag{9}$$

D_p is the drag function, whereas τ_p and θ_p are the interparticle normal stress and particle volume fraction described in Eqs. (10) and (11), respectively. The right-hand side of the acceleration equation represents the following terms: aerodynamic drag, pressure gradient, gravitational acceleration, and gradient in the interparticle stress, τ_p. This stress is based on the particle volume fraction, θ_p, and is given as [27]:

$$\tau_p = \frac{10P_s\theta_p{}^{\beta}}{max[\theta_{cp} - \theta_p, \varepsilon(1-\theta_p)]} \tag{10}$$

P_s and θ_{cp} in Eq. (10) represent pressure constant and close-pack volume fraction, respectively, while ε is a very small number included to prevent the occurrence of singularity as the solid fraction approaches close pack. θ_p is given by

$$\theta_p = \iiint \phi V_p dV_p d\rho_p d\boldsymbol{u}_p \tag{11}$$

V_p is the particle volume and changes in pressure and density are computed using the ideal gas equation.

Secondly, interphase momentum transfer (**F**) represents the rate of change of gas phase momentum due to the presence of particles. It couples the gas phase motion to particle loading and distribution. The interphase momentum transfer in the gas phase momentum equation is given by

$$\boldsymbol{F} = \iiint \phi V_p \rho_p \left[D_p\left(\boldsymbol{u}_g - \boldsymbol{u}_p\right) - \frac{1}{\rho_p}\nabla P\right] dV_p d\rho_p d\boldsymbol{u}_p \tag{12}$$

iv. Drag model

When modelling multiphase flows involving solid particles dispersed in a gas, an accurate representation of drag force is crucial. Drag function, D_p, significantly impacts the momentum exchange between phases through the particle acceleration and interphase momentum transfer terms. Several empirical drag models have been developed to calculate the drag coefficient based on particle and flow properties. Ideal selection depends on the flow regime and desired predictive accuracy. In this study, a modified energy minimization multiscale (EMMS) drag model was adopted. Moreover, this drag model have been successfully applied in previous simulations of SE-SR in fluidised bed systems using a different CFD modelling approach [28–30].

The EMMS-Yang model is suitable for bubbling and turbulent fluidised beds as it accounts for variations in voidage [31]. This modified EMMS model, based on the works of Yang et al. [32] and Li and Kwauk [33], reflects the heterogenous structure of a gas–solid system. Rather than using an empirical drag law, EMMS solves for forces by minimising the total energy of the system, including contributions from potential, kinetic and interfacial energies [33]. This allows the model to account for the complex flow patterns within the voids and drag forces arising from frictional interactions between fluid and solid phases across finite contact areas. It avoids empirical constants and applies over a wide range of operating conditions using only particle properties and volume fraction, θ, as inputs. Yang et al. [32] derived an analytical solution for the EMMS drag law that is more computationally efficient. Thus, the modified EMMS or EMMS-Yang model is adopted. The constants, c, in equations 56 and 57 were generated from the experiment of Li and Kwauk [33].

Table 2
Summary of heat transfer model equations.

Parameters	Expressions	Equation
Heat transfer coefficient	$h_{fw} = h_l + f_d h_d f_d = 1 - e^{-10(\theta_p/\theta_{cp})}$	16
Lean gas phase heat transfer coefficients	$h_l = \left(\left(c_0 \mathrm{Re}_L^{n_1} \mathrm{Pr}^{n_2} + c_1\right)\frac{k_g}{L} + c_2\right), \frac{\mathrm{W}}{\mathrm{m}^2\cdot\mathrm{K}}$	17
Dense particle phase heat transfer coefficients	$h_d = \left(c_0 \mathrm{Re}_p^{n_1}\frac{k_g}{d_p}\right), \frac{\mathrm{W}}{\mathrm{m}^2\cdot\mathrm{K}}$	18
Fluid-to-particle heat transfer	$h_p = \left(\left(c_0 \mathrm{Re}_p^{n_1} \mathrm{Pr}^{0.33} + c_1\right)\frac{k_g}{d_p} + c_2\right), \frac{\mathrm{W}}{\mathrm{m}^2\cdot\mathrm{K}}$	19

$$D_p = \frac{9}{2}\frac{\mu_f}{\rho_p r_p^2} C_d \tag{13}$$

$$C_d = \begin{cases} \dfrac{1}{18\theta_f}\left(c_0\dfrac{\theta_p}{\theta_g} + c_1 \mathrm{Re}\right)\theta_g < 0.74 \\ (c_2 + c_3 \mathrm{Re}^{n_0})\omega\theta_g \geq 0.74 \text{and } \mathrm{Re} < 1000 \\ c_4\dfrac{\mathrm{Re}}{24}\omega\theta_g \geq 0.74 \text{and } \mathrm{Re} \geq 1000 \end{cases} \tag{14}$$

$$\omega = \begin{cases} c_5 + \dfrac{c_6}{4(\theta_g + c_7)^2 + c_8} 0.74 \leq \theta_g < 0.82 \\ c_9 + \dfrac{c_{10}}{4(\theta_g + c_{11})^2 + c_{12}} 0.82 < \theta_g \leq 0.97 \\ c_{13} + c_{14}\theta_g 0.97 < \theta_g \leq 1 \end{cases} \tag{15}$$

v. Heat transfer model

Heat transfer from fluid to particles and wall was calculated using fluid-to-particle and convective fluid-to-wall heat transfer models, respectively. For the fluid-to-wall heat transfer, the local time-averaged heat transfer coefficient, h_{fw}, is calculated by weighting the relative contributions of the lean gas and dense particle phases' heat transfer coefficients. The general equations for the lean gas (l) and dense particle (d) phases' heat transfer coefficients are presented in Eqs. (17) and (18), respectively. The values of c_0, c_1 and c_2 in both equations were obtained from [34]. On the other hand, the fluid-to-particle heat transfer is modelled based on correlation in Eq. (19), with coefficient values taken from [35]. These coefficients, c_0, c_1, c_2 in Eq. (17) and Eq. (19) were taken as 0.46, 3.66, 0 and 0.37, 0.1, 0, respectively. Summary of the heat transfer model equations are presented in Table 2.

2.2.2. Kinetic models

In this study, two representative kinetic schemes were applied – steam methane reforming and carbonation. The steam methane reforming (SMR) model describes the reactions between methane and steam to produce hydrogen and CO_2. The carbonation reaction involves a reversible reaction, where CO_2 reacts with CaO-based sorbent (dolomite) to form calcium carbonate. Modelling this reaction accurately captures carbon dioxide using dolomite sorbents.

i. SMR kinetics

Several kinetic models have been proposed in the literature to simulate SMR processes. There are two widely used schemes developed by Numaguchi and Kikuchi (NK) [36] and Xu and Froment (XF) [37], due to their predictive capabilities. For this study, the NK kinetic model was selected for the following key reasons. First, it offers a simpler formulation compared to some alternatives, avoiding potential errors from numerous kinetic parameters. Additionally, a prior comparative study by Quirino et al. [38] found the NK approach demonstrated relatively high accuracy in modelling reforming reactions. It also exhibited lower numerical instability compared to other evaluated schemes. Stability is important for rigorous multiphase simulations. Given its validation in previous works and simplicity while still adequately representing chemical kinetics, the NK kinetic mechanism provided a suitable basis for the present study. Using its formulation, the steam reforming and water–gas shift (WGS) reactions occurring in SE-SR processes can be characterised as follows:

$$\mathrm{SMR}: \mathrm{CH_4} + \mathrm{H_2O} \leftrightarrow 3\mathrm{H_2} + \mathrm{CO} \qquad \Delta \mathrm{H}^0_{298} = +206\mathrm{kJ/mol} \tag{20}$$

$$\mathrm{WGS}: \mathrm{CO} + \mathrm{H_2O} \leftrightarrow \mathrm{H_2} + \mathrm{CO_2} \qquad \Delta \mathrm{H}^0_{298} = -41\mathrm{kJ/mol} \tag{21}$$

A hybrid rate equation for the reactions is obtained by Numaguchi and Kikuchi [36] based on Langmuir-Hinshelwood and power rate law, and is expressed as:

$$r_{SMR} = \frac{k^0_{SMR}\hat{\mathrm{A}}\cdot exp(-\frac{E_{SMR}}{\mathscr{R}T})(p_{\mathrm{CH_4}}p_{\mathrm{H_2O}} - \frac{p_{\mathrm{CO}}p^3_{\mathrm{H_2}}}{K_{SMR}})}{p^{1.596}_{\mathrm{H_2O}}}, [\mathrm{kmol}/(\mathrm{kg_{cat}}\ \mathrm{s})] \tag{22}$$

$$r_{WGS} = \frac{k^0_{WGS}\hat{\mathrm{A}}\cdot exp(-\frac{E_{WGS}}{\mathscr{R}T})(p_{CO}p_{H_2O} - \frac{p_{CO_2}p_{H_2}}{K_{WGS}})}{p_{H_2O}}, [\mathrm{kmol}/(\mathrm{kg_{cat}}\ \mathrm{s})] \tag{23}$$

Kinetic parameters k^0_{SMR}, k^0_{WGS}, E_{SMR}, E_{WGS}, K_{SMR}, and K_{WGS} were obtained from Numaguchi and Kikuchi [36] and Hou and Hughes [39], and are presented in Table 3.

ii. Carbonation kinetics

The carbonation model proposed by Sun et al. [40] for dolomite and limestone sorbents was adopted for this study, as it has been successfully applied in similar research concerning SE-SR process [21]. The grain model used to describe the carbonation reaction considers how grain size distribution changes with the reaction. This level of detail is important, as the changes in grain size can influence product formation. Furthermore, the Sun et al. [40] model has demonstrated a remarkable capability in capturing the abrupt reduction in carbonation reaction rates that is often observed using CaO-based sorbent [41]. This phenomenon can have a profound impact on the overall performance of the sorbent material. The rate equation is given in terms of conversion and expressed below:

$$r_c = \frac{dX}{dt} = k_C\left(P_{co_2} - P_{co_{2,eq}}\right)^n S(1 - X_{CaO}) \tag{24}$$

Where X_{CaO} is the conversion of CaO defined as:

Table 3
Arrhenius parameters, activation energies and equilibrium constants for the reforming and shift reactions [36].

	k^0	E_a(kJ/mol)	K
SMR	2.634×10^2, $\left[\frac{kmol}{(\mathrm{kg_{cat}}\ atm^{0.404}s)}\right]$	106.870	$1.167 \times 10^{13} exp\left(-\frac{26830}{T}\right)$, $[atm^2]$
WGS	0.248, $\left[\frac{kmol}{(\mathrm{kg_{cat}}\ atms)}\right]$	54.531	$1.767 \times 10^{-2} exp(\frac{4400}{T})$

$$X_{CaO} = \frac{\text{reacted CaO moles}}{\text{total CaO moles}} = \frac{[n_{CaO,0} - n_{CaO,t}]}{[n_{CaO,0}]} \tag{25}$$

S is the specific surface area of the sorbent. The surface area for the CaO part in the dolomite sorbent is taken to be $3.1 \times 10^4 m^2/kg_{sorb}$ [40]. For the dolomite carbonation, a first-order reaction was ascertained for $\mathrm{P_{CO_2}} < 10\,\mathrm{kPa}$, whereas a zero-order reaction was reported for $\mathrm{P_{CO_2}} > 10\,\mathrm{kPa}$. Therefore, the carbonation rate constant, k_C, under both conditions is presented in the equation below:

$$k_c = \begin{cases} 1.04 \times 10^{-10} exp\left(\frac{-24000}{\mathrm{RT}}\right) kmol/(m^2 sPa) at\ \mathrm{P_{CO_2}} - \mathrm{P_{CO_2,eq}} \leq 10kPa; n = 1 \\ 1.04 \times 10^{-3} exp\left(\frac{-24000}{\mathrm{RT}}\right) kmol/(m^2 s) at \mathrm{P_{CO_2}} - \mathrm{P_{CO_2,eq}} \geq 10kPa; n = 0 \end{cases} \tag{26}$$

The equilibrium pressure, $P_{co_{2,eq}}$, is a function of temperature [42], and is calculated according to the Eq. (27):

$$C_{\mathrm{CO_2,eq}} = \left(\frac{1.462 \times 10^{11}}{T}\right) exp\left(\frac{-19130}{T}\right); P_{\mathrm{CO_2,eq}} = C_{\mathrm{CO_2,eq}} RT[atm] \tag{27}$$

iii. Calcination model

As $CaCO_3$ particles decompose during calcination, their size decreases due to the diffusion of CO_2 from the interior to the surface. The changing grain size model considers how grain size distribution changes with the reaction while incorporating the unreacted shrinking core model to provide a more accurate representation of diffusion control compared to simpler models [43]. Garcia-Labiano et al. [44] developed a changing grain size model based on the dolomite particles' granular texture while accounting for internal diffusion limitations. They suggested using the well-known Langmuir–Hinshelwood model to explain the calcination mechanism. Their model took into consideration the diffusion and reaction of gases within a particle's differential volume and was represented using a two-step Langmuir–Hinshelwood mechanism. The first step involves decomposition of $CaCO_3$ to CaO and chemisorbed CO_2, whereas in the second step, CO_2 desorbs from the active site. Their model provided a good representation and fit to experimental data for dolomite across various operating conditions tested; therefore, it was adopted in this simulation. The calcination reaction is a function of CO_2 partial pressure and is given by

$$R_{calc} = k_c S_e(1 - \theta)\left(1 - \frac{P_{\mathrm{CO_2}}}{P_{co_{2,eq}}}\right)\left[\frac{\mathrm{mol}}{\mathrm{kgs}}\right] \tag{28}$$

The fraction of occupied active sites (θ) was found to align with the Freundlich isotherm, with the adsorption constant, c, represented via the Arrhenius expression. θ is the fraction of active sites occupied by CO_2 and is a function of CO_2 partial pressure and adsorption constant, according to the Freundlich isotherm expression below:

$$\theta = c\sqrt{P_{CO_2}} \tag{29}$$

The adsorption constant, c, and the kinetic rate constant, $k_c[molm^{-2}s^{-1}]$, are given by

$$c = c_0 e^{\frac{E_a}{RT}} \tag{30}$$

$$k_c = k_0 e^{\frac{E_c}{RT}} \tag{31}$$

Table 4
Kinetic parameters for the calcination of dolomite [44].

Parameter	Value	Units
E_c	114	$kJmol^{-1}$
E_a	−90	$kJmol^{-1}$
c_0	3.5×10^{-7}	$Pa^{-0.5}$
k_0	29.5	$molm^{-2}s^{-1}$

Consistent with changing grain size models, the reaction surface area is determined by the particle radius, which changes as the reaction progresses. Therefore, the specific surface area of the sorbent, S_e, is based on Eq. (32), where r_0 and r_1 are the initial radius of $CaCO_3$ and the radius of its unreacted core, respectively.

$$S_e = S_0\left(\frac{r_1}{r_0}\right)^2 \tag{32}$$

For simplicity, r_1 is assumed to be independent of the grain's radial position, so that a correlation between $\frac{r_1}{r_0}$ and the unconverted $CaCO_3$ (X_{CaCO_3}) can be determined [45]. Therefore, S_e is estimated in Eq. (33). Additionally, the S_0 is taken to be 9.57×10^3 m^2/kg [44].

$$S_e = S_0(X_{CaCO_3})^{\frac{2}{3}} \tag{33}$$

The equilibrium pressure, $P_{co_{2,eq}}$, is a function of temperature as described by Barin [46], and for a high-temperature calcination process, is calculated according to the equation:

$$C_{CO_2,eq} = \left(\frac{4.137 \times 10^{12}}{T}\right) exp\left(\frac{-20474}{T}\right); P_{CO_2,eq} = C_{CO_2,eq}RT[atm] \tag{34}$$

The kinetic parameters used in the calcination sub-model are provided in Table 4.

2.2.3. Numerical solutions and model settings

The Eulerian conservation equations for the gas phase are solved using the finite volume method, while the particle phase equations are solved using computational parcels, which follow typical routes in phase space with particle velocities, locations, and sizes as coordinates. Parcel attributes are interpolated onto the Eulerian grid and the implicit approximations to the particle-phase are solved. The local gas velocities, gas pressure gradients, and solids stress gradients are interpolated back to parcel coordinates, and employed in a final explicit update of parcel velocities once the grid equations are solved.

The interpolation of particle properties to and from the Eulerian grid is achieved using interpolation operators. For a rectangular grid where a particle is located at x_p and $x_p = (x_p, y_p, z_p)$, the interpolation operator, S, in the cell centre x-direction takes the form for all nodes, i:

$$S_i^x(\mathbf{x}_p) = \begin{cases} 0 & x_{i-1} \geq x_p, x_p \geq x_{i+1} \\ 1 & x_p = x_i \end{cases} \tag{35}$$

and

$$\sum_i S_i^x(x_P) = 1 \tag{36}$$

The operators are defined in a similar way for face centre directional interpolation operators, with properties as:

$$S_{i+1/2}^x(\mathbf{x}_p) = \begin{cases} 0 & x_{i-1/2} \geq x_p, x_p \geq x_{i+3/2} \\ 1 & x_p = x_{i+1/2} \end{cases} \tag{37}$$

and

$$\sum_\xi S_\xi^x(x_P) = 1 \tag{38}$$

for all face nodes, ξ.

Table 5
Model parameters and settings used in the CPFD software.

Parameters	Values	Units
Maximum momentum redirection from collision	40	%
Normal-to-wall momentum retention	0.85	–
Tangent-to-wall momentum retention	0.85	–
Courant–Friedrichs–Lewy (CFL) range	0.8 – 1.5	–
Time step	0.001	s
Simulation time	200	s
Averaging start time	100	s

Table 6
Case description for the simulated reactors.

Cases	Geometry	Catalyst-to-sorbent volumetric ratio (Reformer)	Catalyst-to-sorbent mass ratio (Reformer)
CFB1-0.25	1	0.25	0.3
CFB1-1	1	1	1.3
CFB1-4	1	4	3
CFB2-0.25	2	0.25	0.3
CFB2-1	2	1	1.3
CFB2-4	2	4	3

In three dimensions, $\boldsymbol{x}_p$ is interpolated to eight grid nodes. The y and z operators follow similar patterns and are all independent of their counterpart coordinates. The motion of particles in the continuum fluid momentum equation is coupled through an implicit coupling approach, in the numerical scheme. This approach results in the product of the particle to grid interpolation operators.

On the other hand, the grid-to-particle interpolation operator is used to interpolate the grid quantities back to the individual particle positions. The gradient of the grid-to-particle interpolation operator is important for calculating the forces acting on the particles. These force calculations then allow for updating the particle properties, during the next timestep of the simulation. The grid property (Q) mapped to particle location ($\mathbf{x}_p$), in support of the interpolation operator (S_ξ), is presented in equation (39), while the gradient of the particle property is given in Eq. (40).

$$Q_p = \sum_{\xi=1}^{N} S_\xi(x_P)Q_\xi \tag{39}$$

$$\nabla Q_p = \sum_{\xi=1}^{N} \nabla S_\xi(x_P)Q_\xi + \sum_{\xi=1}^{N} S_\xi(x_P)(\nabla Q)_\xi \tag{40}$$

Detailed explanation for the product and gradient of interpolation operators for three-dimensional calculations are provided by Snider [27].

The model settings used in the simulation are presented in Table 5. Maximum momentum redirection from collision refers to the largest possible change in momentum that can occur when two particles collide. Tangent-to-wall momentum retention refers to how much of a particle's tangential momentum is maintained after colliding with a wall boundary, while normal-to-wall momentum retention similarly describes the degree to which normal momentum is conserved upon particle–wall collisions [25]. The blended acceleration model (BAM) was also set for the simulation. The BAM in dense polydisperse granular flows accounts for inhibited relative motion between differently sized particles in sustained contact. BAM calculates particle acceleration as a blend of approaches – an averaged value in dense packed regions where particles adhere collectively, and independent motion in dilute areas [47]. This better represents inter-particle interactions across flow regimes, improving predictions of segregation behaviour during fluidisation simulations.

Table 7
Operating conditions and model settings for the simulation of SE-SR of methane in CFB reactor.

Parameters	Value	Unit
Total volume of solids in the system	0.160	L
Bed voidage	0.55	–
Catalyst and sorbent particle size range	90 – 200	μm
Catalyst density	2200	kg/m^3
Sorbent density	1500	kg/m^3
CaO/MgO concentration	60/40	wt%
Catalyst thermal conductivity [52]	0.33	W/(mK)
Sorbent thermal conductivity (at room temperature) [53,54]	15	W/(mK)
Reformer temperature	873	K
Calciner temperature	1173	K
Reactor pressure	1	atm

The Courant–Friedrichs–Lewy (CFL) condition is a fundamental stability criterion in CFD. The CFL criterion relates the time step size, grid cell size and propagation speed, stating the time step must be small enough such that information cannot propagate further than the size of one cell in a single iteration [48]. If the CFL number is too high, information moves faster than waves, causing numerical dispersion errors. But too low (<0.1) wastes computational resources without benefiting stability.

2.2.4. *Operating conditions and assumptions*

As seen in Table 6, three scenarios were considered to evaluate system performance under conditions simulating sorbent degradation and catalyst deactivation over time. A low catalyst loading scenario (volume ratio: 0.25) was used to mimic gradual catalyst deactivation by providing less active catalytic sites. This allows studying how conversion rates decline with lower catalytic activity and whether reforming and carbonation reactions can still sufficiently proceed. A high catalyst loading but low sorbent addition scenario (volume ratio: 4) was used to simulate the effects of sorbent degradation by providing less sorbent. This scenario can provide insights into how product selectivity shifts as sorbent capacity decreases. Whilst very few catalyst deactivation models for SMR still exist [49], a reduced loading approach provides insights without additional complexity. Further, no validated deactivation models currently consider the SE-SR condition. An intermediate, baseline scenario with equal catalyst and sorbent addition was also evaluated.

Also, the two computational geometries – CFB1 and CFB2 – were designed, where CFB1 and CFB2 have equal bed volumes. Each geometry was then modelled at three different scenarios of catalyst to sorbent volume ratios, as seen in Table 6. This resulted in six total cases to be simulated, each parameterised with a range of catalyst to sorbent ratios. These cases were configured to provide insight into how both structural modifications and material loading ratios could influence hydrodynamics and reaction kinetics within the dual CFB reactor system. Assessing the SE-SR performance across these varied conditions, will help improve the understanding of the impacts of catalyst-to-sorbent ratios and invariably catalyst deactivation and sorbent degradation, in order to maximise the system's long-term operation and resilience against these expected modes of decline.

The initial operating conditions for the system were taken from Arstad et al. [50], to obtain consistent results for model validation and evaluation. Pressure and velocity boundary conditions were used to model the flow in the reactor. The pressure boundary condition was specified at the outlet of the reactor, and the velocity boundary condition was specified at the inlet of the reactor. The fluidised bed system was modelled under adiabatic condition, without the added complexity of heat losses in and out. Due to the small contribution of radiation expected for such small-scale system, compared to conduction and convection, radiative heat transfer was ignored [51]. Physical properties and operating conditions of the fluidising gas and particles are listed in Table 7.

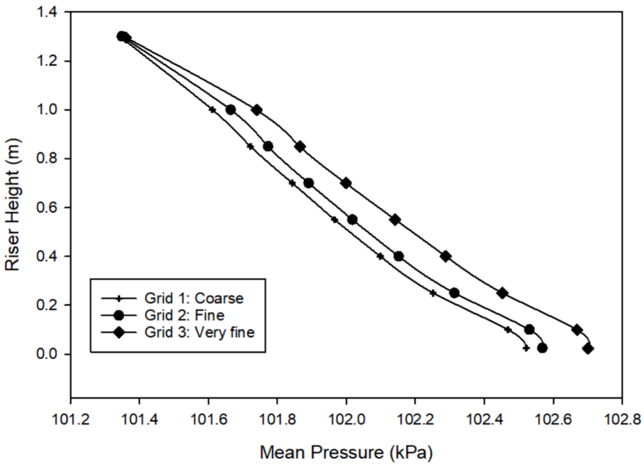

Fig. 2. Comparison of the transport riser pressure profiles for the different grid cell sizes.

Following the completion of the simulation, product gas compositions from the exit stream were obtained on a dry basis, with methane conversions and hydrogen yields calculated from Eqs. (41) and (42), respectively. The CO$_2$ capture efficiency (CCE) in Eq. (43) is based on carbon mass balance around the reformer, while Eq. (44) presents the reformer's process efficiency (PE).

$$X_{CH_4} = \left(1 - \frac{x_{CH_4,out}}{x_{CH_4,in}}\right) \times 100\% \tag{41}$$

$$Y_{H_2} = \frac{x_{H_2,out}}{4x_{CH_4,in}} \times 100\% \tag{42}$$

$$CCE = \left(\frac{x_{CH_4,in} - (x_{CO_2,out} + x_{CH_4,out} + x_{CO,out})}{x_{CH_4,in} - (x_{CH_4,out} + x_{CO,out})}\right)_{reformer} \times 100\% \tag{43}$$

$$PE = \left(\frac{m_{H_2} \times LHV_{H_2}}{(m_{CH_4,in} \times LHV_{CH_4})}\right) \times 100\% \tag{44}$$

2.3. *Grid independence study*

A grid independence study was conducted to evaluate the effect of cell size on the accuracy of the reactor model. Three different mesh sizes were chosen – 1 million cells (coarse), 1.2 million cells (fine) and 1.5 million cells (very fine). Simulations were run using each mesh size and pressure profiles along the vertical height of the connecting transport riser were examined and compared. This transport riser was chosen as the basis for comparison since it is common to both geometries. Fig. 2 shows the results of the pressure profiles.

With 1 million cells, the pressure profile showed higher pressure at the bottom, which reduced along the height of the riser. When the mesh was refined to 1.2 million cells, the pressure profile appeared the same with fewer irregular variations. Increasing the mesh size further to 1.5 million cells did not lead to significant changes in the pressure profile. The profiles matched very closely, suggesting that further mesh refinement beyond 1.2 million cells was not providing additional insight into the flow behaviour. The percent difference in pressures between the coarse and fine cell meshes ranged from 0.01 % – 0.06 % at different points, showing a noticeable effect of mesh size. However, the difference was only 0.012 % – 0.13 % when comparing the fine and very fine cell meshes. This indicated that the solution was relatively independent of further mesh refinement and 1.2 million cells was providing an

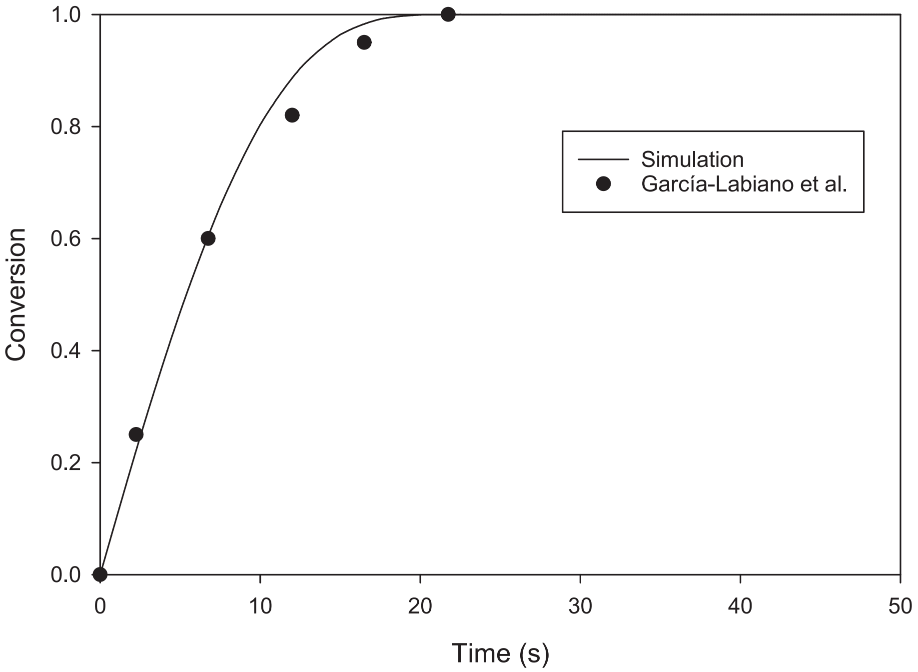

Fig. 3. Comparison of calcination conversion level from the simulation case with literature data, both at 1 atm, 1123 K and 0 % CO_2 [44].

appropriately well resolved solution. Based on the pressure profile comparisons, the fine grid was concluded to be a suitable mesh that balanced accuracy with computational cost. While the very fine mesh may have resulted in marginal increase in mean pressures, the minimal improvement did not justify the increased simulation time.

3. Results and discussion

Simulation of the bench-scale dual CFB reactor in the CPFD program began with the random particle initialisation of mass in the domain, where the total mass of particles in the system was approximately 1.5 kg. This initial particle randomisation is important to properly set up the computational model before the dynamic simulation captures how the particles interact with the flowing gas streams. The simulation was run for 200 s for each of the cases defined for the dual CFB reactor system. This simulation time was sufficient to capture multiple cycles of particle flow and mixing within the two interconnected reactor vessels being modelled. The simulation results over the 200 s period were then analysed for each of the cases to evaluate system hydrodynamics and parameters of interest for the bench-scale SE-SR system. This section reports the results of the simulation.

3.1. Model validation

The calcination kinetics was validated by simulating a unit cube geometry. The unit cube geometry is a simplified model replicating the operating conditions (pressure, temperature, particle size and density) of the thermo-gravimetric analyser (TGA) experiment conducted by Garcia-Labiano et al. [44]. This single-cell case was adopted to simplify the simulation setup, reduce the computational time, and make it easier to identify and troubleshoot any issues with the calcination reaction rates. The cube was filled with 0.4 – 0.6 mm diameter of half-calcined dolomite ($CaCO_3 \cdot MgO$) particles at atmospheric pressure, in a nitrogen environment and 0 % CO_2 partial pressure. The reaction temperature was set at 1123 K and the simulation was run for 50 s for complete calcination.

A conversion-time plot for the calcination process was generated from the simulation and compared with the experimental result from Garcia-Labiano et al. [44], as shown in Fig. 3. The plot shows that complete calcination of the carbonated dolomite particles was achieved after 20 s in the simulation compared with ~22 s observed in the experiment. Since the simulation and experimental results are close, the kinetic model is considered to be suitable for further adoption in the CFB

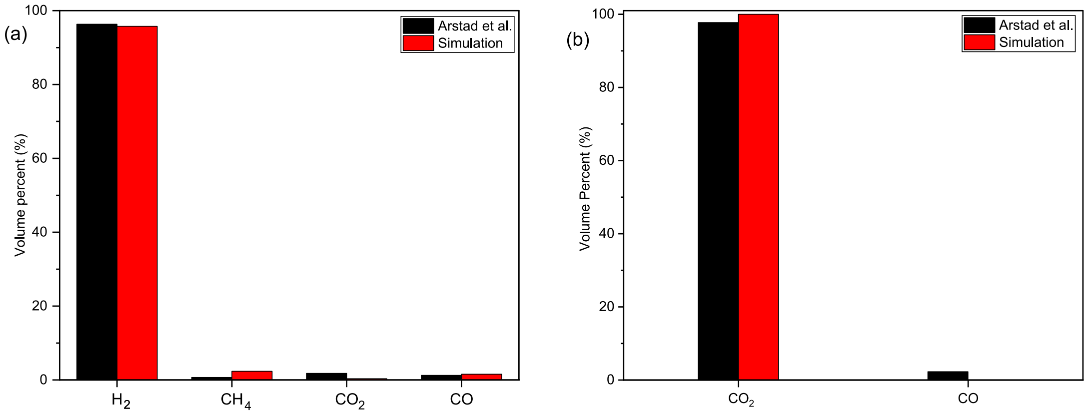

Fig. 4. Comparison of the (a) reformer and (b) calciner product compositions from the simulation case with literature data [50].

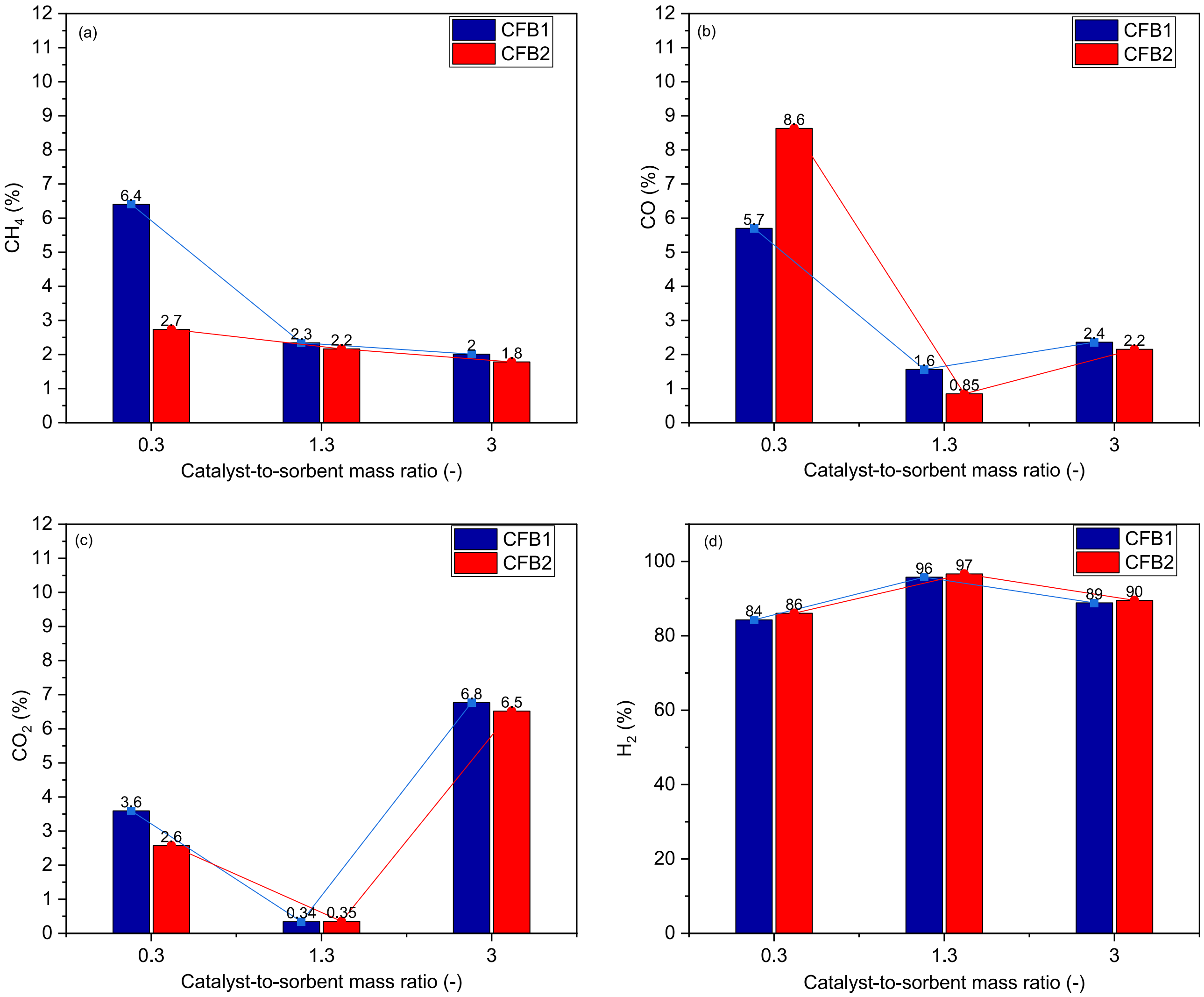

Fig. 5. Composition of (a) CH_4 (b) CO (c) CO_2 and (d) H_2 at the reformer exit for designs 1 (Blue bar with blue trendlines) and 2 (Red bar with red trend lines) at catalyst-to-sorbent mass ratios of 0.3, 1.3 and 3. (For interpretation of the references to colour in this figure legend, the reader is referred to the web version of this article.)

reactor modelling.

Following the validation of the calcination reaction model, it was integrated into the CFB reactor model and the full-loop system was validated. To validate the accuracy of the SE-SR in dual CFB reactor simulation model, a comparison was made between the experimental data by Arstad et al. [50] and results from the simulation case – CFB1-1. This case was used because it had similar geometric parameters and operating conditions (including pressure, temperature, particle size and density) representing the actual bench-scale reactor. The simulated reformer/carbonator product composition for the last 10 s, after 200 s simulation time, was extracted and averaged from the CFB1-1 case data and compared with the experimental compositions on a dry volume (%) basis. If the simulated composition matches the experimental data, it indicates that the underlying reaction mechanisms and hydrodynamics modelled in the simulation are likely capturing the actual chemistry taking place.

Fig. 4a shows the model generally captured the product compositions from the reformer/carbonator, with minor deviations. The simulation underpredicted the H_2 and CO_2 outlet compositions by 0.56 % and 1.44 % respectively, while overpredicting CH_4 and CO by 1.67 % and 0.33 %, respectively. Fig. 4b illustrates the model also adequately predicted the calciner outlet compositions. The trends in all compositions agreed well between the simulation and experimental data for both reactors. While some compositions exhibited under or overpredictions of less than 2 %, the modelling approach was still able to capture the overall product compositions leaving the reactors.

The slight differences in compositions between the simulation and literature data could be due to the kinetic model adopted in the simulation. Past studies on SMR kinetics developed and proposed different reaction mechanisms for steam methane reforming [38]. Xu and Froment [37] proposed that CO_2 is formed by both water–gas shift and steam reforming reactions, and includes a third overall reaction producing CO_2 and H_2. In contrast, Numaguchi and Kikuchi's (NK) model [36] used in this study omitted this additional reaction pathway, which has recently been reported to predominate at lower temperatures [38]. Nevertheless, the NK model has shown good prediction with experimental for SE-SR studies [14,29,55]. Having successfully validated the model against experimental data, the CPFD model was then used to conduct further studies.

3.2. Product distribution and performance at various solids loadings

Fig. 5a shows that there is a significant impact of the selection of catalyst-to-sorbent ratio. Improving catalyst loading, and invariably catalyst-to-sorbent ratio, reduced the methane content in the outlet streams by promoting higher methane conversion. Fig. 5a also

Table 8
Composition of the product gas from the reformer for the various catalyst masses, in the absence of sorbent.

Catalyst mass (kg)	CH_4 (%)	CO (%)	CO_2 (%)	H_2 (%)	CH_4 Conversion (%)
0.014	8.44	4.49	14.72	72.35	84.43
0.034	4.91	5.55	14.58	74.96	90.15
0.054	4.37	5.76	14.52	75.36	91.23
Equilibrium (CPFD model)	0.18	7.74	13.75	78.32	99.00
Equilibrium (Aspen model)	0.38	7.00	14.32	78.30	98.34

demonstrates that lower catalyst mass led to higher methane levels in the product stream as a result of decreased methane conversion, approximating the effects of losing catalytic activity over time. Lowering the catalyst loading simulated the impact of gradual catalyst deactivation by reducing the number of active catalyst sites available for reforming reactions. [49].

Although lower catalyst loading impacted methane levels, the relatively low outlet compositions of CO and CO_2 in Fig. 5b and Fig. 5c, respectively, indicate the presence of sorbent still benefitted the process. Prior to developing the SE-SMR model, batch simulations without sorbent produced higher residual methane as well as CO and CO_2. The SMR reaction without CaO sorbent was simulated in a reactor filled with catalyst particles for the three catalyst masses used in each of the C-S mass ratios. The composition of the product streams for the three cases, in the absence of CaO sorbent, are presented in Table 8. The data in Table 8 shows that increasing the catalyst mass improved activity, as evidenced by decreasing methane content and increasing hydrogen content in the product gas.

Table 8 also includes data of the equilibrium composition of the SMR reaction from the CPFD model and validated in a thermodynamic software – Aspen Plus®. Aspen Plus V14 was used to model the equilibrium composition by applying the Peng-Robinson equation of state to simulate the RGibbs reactor, which uses the Gibbs free energy minimization to determine the reactor outlet composition at chemical equilibrium [56]. At S/C ratio, temperature, and pressure of 4, 873 K, and 1 atm, respectively, the equilibrium compositions from the Aspen Plus and CPFD models are comparable, as seen in Table 8. Comparing the product gas compositions predicted at different catalyst loadings against the equilibrium compositions shows that increasing the catalyst mass from 0.02 kg to 0.05 kg enabled closer approach towards equilibrium composition, which is consistent with faster reaction kinetics expected from more available active sites. However, increasing catalyst mass above 0.034 kg did not show any appreciable change in both CH_4 content in the outlet stream and methane conversion. In addition, the CPFD model still predicts some deviation from complete thermodynamic equilibrium even at 0.05 kg loading, due to their different calculation methods and thermodynamic databases. However, as Fig. 6 demonstrates, combining the catalyst with sorbent significantly enhanced the product composition compared to catalyst alone, even under conditions of reduced catalytic activity.

Whilst the CO_2 sorbent was able to enhance the product composition, Fig. 5b shows relatively high composition of CO specifically under the low catalyst loading condition. For instance, in CFB1, the CO level initially decreased from 5.70 % to 1.56 % as the C-S ratio was increased from 0.3 to 1.3, but then increased again to 2.36 % at a ratio of 3. A couple of reasons could explain this non-linear trend. At C-S mass ratio of 0.3, the high observed CO concentration can be attributed to the slow CO_2 sorption kinetics from the unfavourably low CO_2 driving force under the current operating conditions. Literature indicates that for rapid CO_2 sorption kinetics, the CO_2 partial pressure needs to be higher than the equilibrium value to provide adequate chemical potential for carbonation using CaO [40]. In this case, the low partial pressure was likely below the threshold needed for appreciable uptake rates. However, this still allowed some methane to be converted to CO via the steam reforming reactions while increasing the CO levels leaving the reactor. Another reason for the relatively high CO in the product stream could be the low water–gas shift activity resulting from the low catalyst loading. Since more methane is being converted following CO_2 sorption, the water–gas shift activity will go even lower, limiting CO conversion to CO_2, due to the low catalyst loading. The high level of CO observed for this low C-S ratio is not peculiar to this study. Chanburanasiri et al. [57] investigated the effects of varying Ni catalyst loading in a Ni/CaO multifunctional particle at 873 K, 1 atm, and a steam-to-carbon ratio of 3. They reported that increasing Ni loading to 12.5 wt% yielded 80 % H_2, 6 % CO, and 2 % CO_2, though the CaO was reported to having only 45 % of its pure component sorption capacity. Other reports have also highlighted the role of catalysts in driving water–gas shift reactions, even in enhanced conditions [58–60]. Thus, a certain level of catalytic activity is essential to promote the water–gas shift reaction and adequately convert CO to CO_2. Further, the CO levels observed at C-S mass ratios of 0.3, 1.3 and 3 provide insight into the relationship between CO levels and C-S ratios. At a C-S ratio of 0.3, representing a low catalyst loading, CO levels remained high, highlighting the need for sufficient catalyst sites to drive the water–gas shift reaction. A C-S ratio

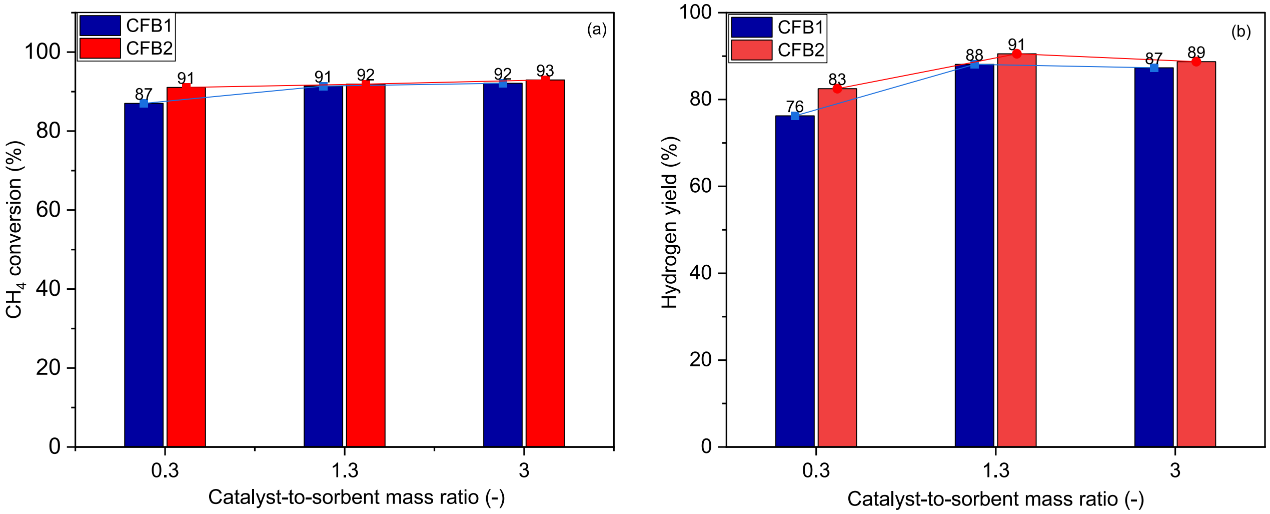

Fig. 6. Methane conversion (a) and hydrogen yield (b) for designs 1 (Blue bar with blue trendlines) and 2 (Red bar with red trend lines) at catalyst-to-sorbent mass ratios of 0.3, 1.3 and 3. (For interpretation of the references to colour in this figure legend, the reader is referred to the web version of this article.)

Table 9
CO_2 capture and process efficiencies for the different cases.

Cases	CCE (%)	PE (%)
CFB1-0.3	80.22	73.13
CFB1-1.3	98.53	87.54
CFB1-3	67.82	86.77
CFB2-0.3	85.98	80.85
CFB2-1.3	98.51	90.76
CFB2-3	69.38	88.29

of 1.3, demonstrating a balanced loading of both catalyst and sorbent, produced lower CO levels, showing the synergistic benefits of the combined solids. Finally, a C-S ratio of 3, equivalent to a low sorbent loading, also resulted in slightly high CO, signifying the importance of adequate sorbent mass to promote equilibrium shifts through sorption.

SE-SR involves continuous cycles of carbonation and calcination, making it prone to sintering and reducing its sorption capacity over time. The reduced mass of CaO sorbent at C-S ratio of 3, in the reformer/carbonator, represents lower sorption capacity and activity as the sorbent degrades. Fig. 5c illustrates how varying the sorbent loading relative to catalyst mass (C-S ratio) impacts the CO_2 concentration in the outlet stream. At low C-S ratios where sorbent mass dominates, higher sorbent levels effectively lowered CO_2 levels through selective sorption. However, comparing the C-S ratios of 0.3 and 1.3, where the sorbent loading was reduced by approximately 39 %, the CO_2 concentration significantly decreased from 3.59 % to 0.34 % and 2.74 % to 0.35 % for reactor CFB1 and CFB2, respectively, despite the lower absolute sorbent mass. This could be due to the improved sorption capability afforded by an increase in the partial pressure of CO_2, as a result of steam methane reforming driven by the presence of additional catalyst at C-S ratio of 1.3. As the mass reduces into the sintered region at C-S ratio of 3, the simulated reduced sorbent capacity results in less CO_2 being captured from the gas stream. This causes CO_2 concentrations to initially decrease then rise again, as shown in the figure. Although, in cases where SE-SR is operated at high pressures, the behaviour of the system under low catalyst loading (0.3) is likely to be different, as high pressures favour sorption of CO_2 [61].

The selective sorption of CO_2 serves to shift the equilibrium of the steam methane reforming reaction in favour of more hydrogen production. As seen in Fig. 5d, despite the low activity observed at C-S of 0.3, there was still an improvement in hydrogen concentration, which increased from 78.32 % at equilibrium to 84.30 % and 86.06 % for CFB1 and CFB2, respectively. This was increased further to 95.75 – 96.64 % at C-S of 1.3, following more CO_2 sorption but reduced to 88.86 – 89.50 % at C-S of 3, due to low sorbent amount. At the low C-S ratio of 0.3 with minimal catalyst, the addition of substantial sorbent did not increase hydrogen concentrations beyond the level achieved at the lower sorbent loading of C-S=3. Thus, during periods of poor catalyst activity, simply adding more sorbent does not necessarily enhance performance compared to optimising catalyst loading. The activity of the steam reforming catalyst imposes fundamental limits on hydrogen production that cannot be overcome through sorbent amounts alone when catalyst loading is insufficient. Additionally, Table 8 shows that above a catalyst loading of 0.034 kg (without sorbent), corresponding to 55 wt% (total solids) of catalyst interspersed with sorbent, there was minimal gains in hydrogen concentration. This suggests that in the presence of sufficient or optimum catalyst mass, a sorbent (CaO.MgO) loading between 45–76 wt% (27–45 wt% CaO content) was adequate for improving hydrogen yield. Literature suggests CaO content of around 30 wt% for stable CO_2 sorption performance, aligning with these results [62–64].

Thus far, the impact of varying catalyst and sorbent loadings on component concentrations – CH_4, CO, CO_2 and H_2 in the product gas has been analysed. However, the primary value of SE-SR lies in its ability to produce high yield and high purity hydrogen. Adjusting parameters like C-S ratio not only affect equilibrium conditions through sorbent mediation, but also influence methane conversion and hydrogen yields. Fig. 6 builds upon the findings of Fig. 5 by showing how the different loading schemes corresponding to various C-S ratios impacted the methane conversion and hydrogen yield. In Fig. 6a, the lower methane conversion observed under the low catalyst loading condition aligns with literature showing reduced conversion at lower catalyst activities [65,66]. This is attributable to slower reaction kinetics with fewer active sites. Despite the poor catalyst activity, adding sorbent still improved methane conversion from ~84 % (without sorbent) to 87–91 %. Increasing the sorbent amount (C-S=0.3) gave comparable improvements in methane conversion to those achieved by using relatively high catalyst loading – low sorbent loading (C-S=3). For hydrogen yield in Fig. 6b, low catalyst loading – high sorbent loading (C-S=0.3) was most detrimental to hydrogen yield, with much higher yield attained with lower sorbent loading (high catalyst loading). This is similar to the hydrogen concentration trend and indicates that while sorbent provides equilibrium benefits, sufficient catalyst activity is essential for maximising hydrogen production rate and yield.

The C-S ratio significantly impacts CO_2 capture efficiency (CCE) and process efficiency (PE) in both CFB1 and CFB2 reactors. Table 9 summarises these efficiencies for the various C-S ratios. In CFB1, reducing

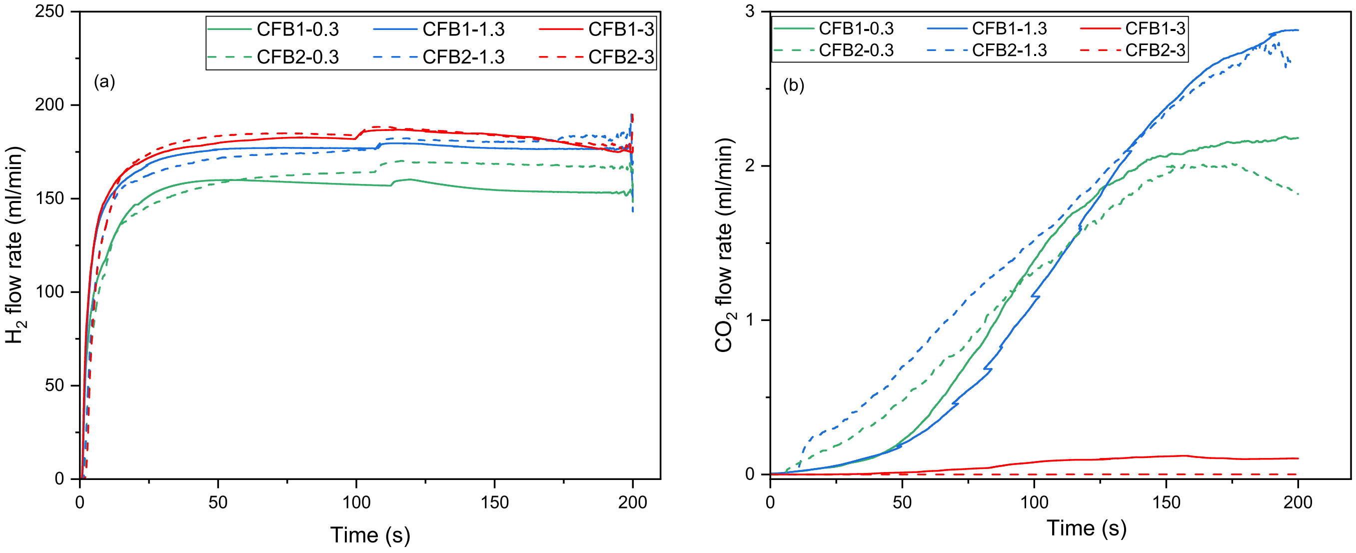

Fig. 7. Flow rate of (a) hydrogen produced from the reformer/carbonator and (b) CO_2 released from the calciner.

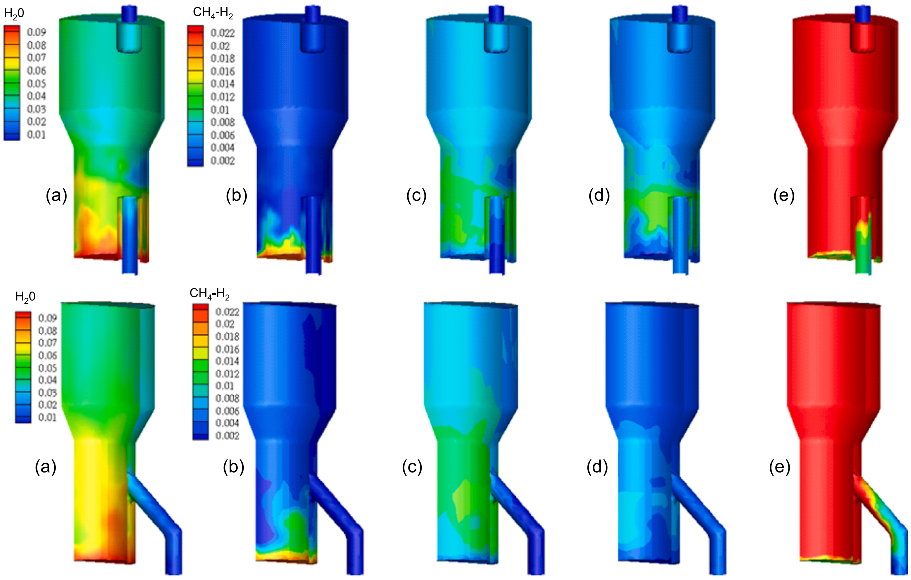

Fig. 8. Contours of (a) H_2O, (b) CH_4, (c) CO, (d) CO_2, and (e) H_2 distributions in the reformer/carbonator of CFB1 and CFB2 bed geometries cut into half axially.

sorbent loading (C-S=3) decreased CCE from 98.53 % at the base ratio (C-S=1.3) to 67.82 %. Similarly, CFB2 showed a CCE reduction from 98.51 % to 69.38 % at C-S=3. Conversely, reduced catalytic activity (C-S=0.3) lowered CCE to 80.22 % in CFB1 and 85.98 % in CFB2, compared to their respective base ratios. For both reactor designs, the lowest CCE occurred at C-S=3, corresponding to low sorbent loading. Process efficiency was lowest at C-S=0.3, where catalyst activity was low. These results indicate that catalyst activity has a more pronounced effect on methane conversion efficiency, hydrogen yield, and process efficiency than on carbon capture efficiency. Within this study's parameters, low sorbent loading impacts carbon capture efficiency, with relatively less influence on methane conversion, process efficiency and hydrogen yield.

The curve in Fig. 7 illustrate the time-dependent production of hydrogen from the reformer/carbonator, and the concomitant CO_2 release from the calciner unit used to regenerate the sorbent. In Fig. 7a, the hydrogen production rate profiles show comparable rates between the C-S ratios of 1.3 and 3 (low sorbent loading) initially. However, the C-S 3 (red curves) starts declining earlier versus C-S 1.3 (blue curves) as the cycle progressed, for both geometries. This is attributable to the insufficient sorbent in the reformer resulting in slower regeneration kinetics and leading to the eventual production decline. The corresponding CO_2 generation trends in Fig. 7b reflect this, with C-S 3 showing delayed onset but later increase slightly in calciner CO_2 release. This means more unused catalyst ends up in the calciner, which is inefficient. Using bifunctional catalysts with integrated sorbent could help mitigate this issue. The earlier CO_2 generation for C-S 0.3 (low catalyst/high sorbent loading) reflects the large sorbent inventory sending more material for regeneration early on. While the C-S=1.3 (blue curves) case begins with a lower calciner CO_2 rate than 0.3, it soon surpasses it as more used sorbent accumulates for regeneration.

As this study also sought to evaluate how the CFB1 (internal outflow pipe) bed geometry design compares with CFB2 (side solids exit), simulations results compared key reactor performance metrics including thermal performance, solids distribution, and product composition between the original and modified geometries across a range of catalyst-to-sorbent (C-S) ratios. The bed volume in both geometries were kept the same for transparent comparison. Beyond simplifying bed geometry to facilitate scale-up studies, one objective of this comparison is to also understand how bed geometry design influence mixing and flow between the interconnected fluidised beds and overall system performance. Bed geometry can affect the hydrodynamics of a system, which in turn, impacts on the heat and mass transfer and overall chemical performance [67]. From the results presented so far, it is clear that both geometries performed slightly similar except for the obvious disparity at C-S of 0.3. Perhaps, the presence of an obstruction (pipe) inside the reactor in CFB1, in addition to reduced catalyst surface area, influenced the methane flow behaviour such that it reaches more height (especially around the pipe area) into the bed before it is substantially converted.

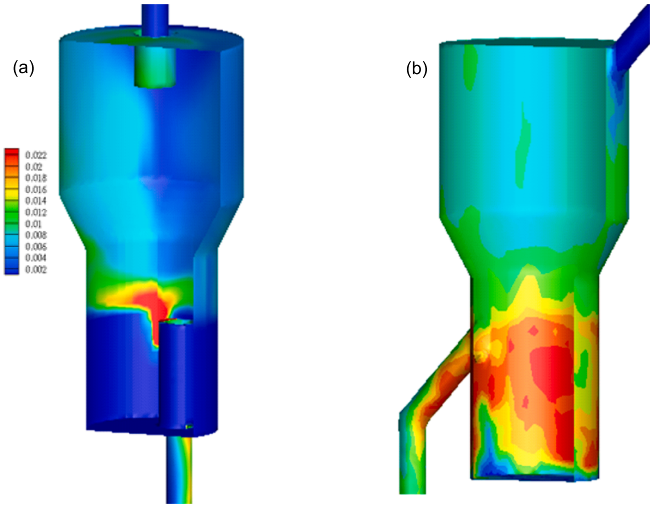

Fig. 9. Contours of CO_2 distributions in the calciner of (a) CFB1 and (b) CFB2 bed geometries cut into half axially.

An analysis of component distributions also shows similar behaviour observed for CO_2 and CO distribution in CFB1 at C-S 1.3, as presented in Fig. 8. Fig. 8 shows the component distribution inside the reformers of both reactor geometries cut in the axial direction at C-S 1.3. For CFB2, there was a slight improvement in consumption of CO_2, which can be attributed to increased usable sorbent surface area and reactants' better access to the surface area, as they were not channelled away around the pipe area like CFB1.

It is interesting to see how CO_2 is distributed within the calciners in Fig. 9 for both bed geometries. CFB2 exhibited a higher CO_2 concentration centred along the reactor axis, indicating preferential gas flow

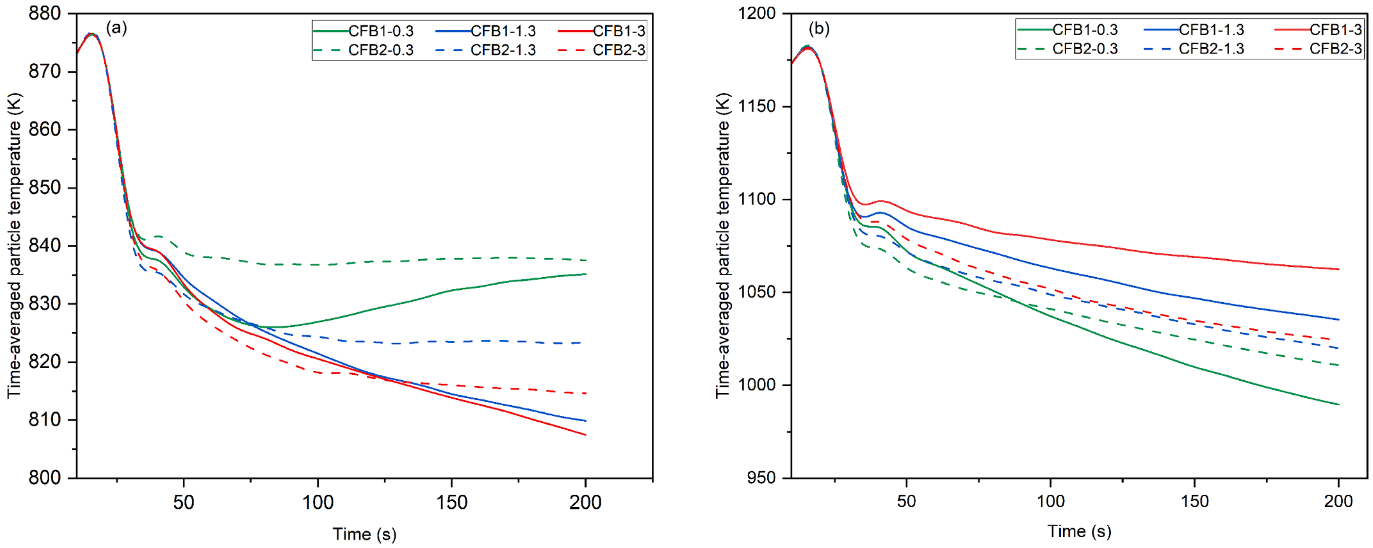

Fig. 10. Time-averaged particle temperatures in the (a) reformer/carbonator and (b) calciner for CFB 1 and 2 at different catalyst-to-sorbent ratios.

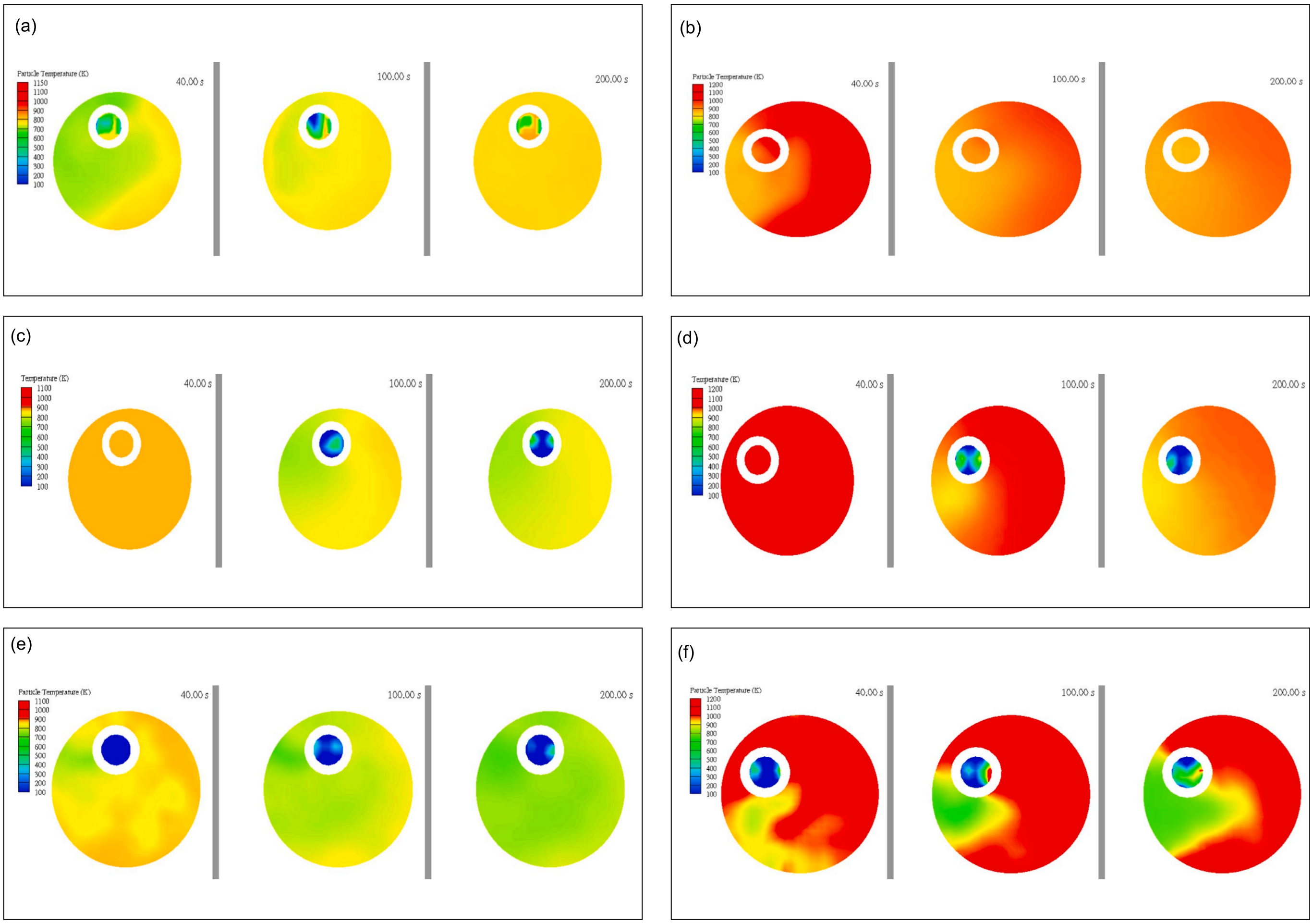

Fig. 11. Contours of temperature distribution mid-bed CFB 1 for catalyst-to-sorbent ratios (a),(b) 0.3 (c),(d) 1.3 and (e),(f) 3 in the reformer/carbonator (a,c,e) and calciner (b,d,f).

through the core region. In contrast, CFB1 featured a more localised accumulation of CO_2 surrounding the top of the internal pipe perimeter. This localised distribution in CFB1 suggests the pipe geometry imposed a degree of directiveness on the local fluidisation patterns, leading to a flow closer to the wall. Bubbles in CFB1 may have been steered toward the open radial slots between the pipe and wall surface.

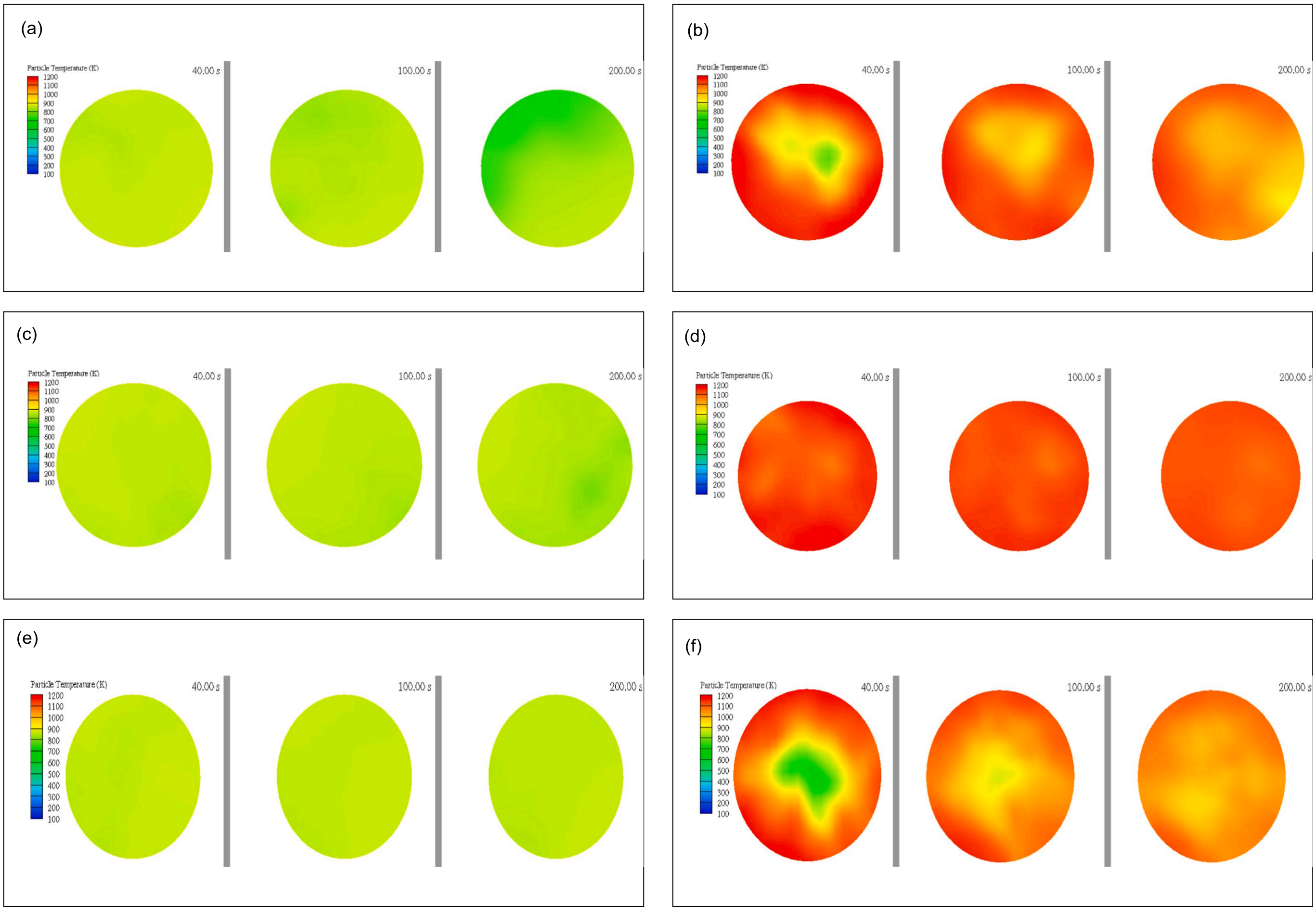

Fig. 12. Contours of temperature distribution mid-bed CFB 1 for catalyst-to-sorbent ratios (a),(b) 0.3 (c),(d) 1.3 and (e),(f) 3 in the reformer/carbonator (a,c,e) and calciner (b,d,f).

3.3. Time evolution and spatial distribution of particle temperature

While operating with a large sorbent inventory helped improve CO_2 capture to an extent as well as increase CO_2 release in the calciner due to more spent sorbent circulation, it came at the cost of higher thermal energy requirements, especially in the calciner. Some studies use excess solid sorbent in the reformer to try to improve the system's thermal neutrality [68–70], but this only marginally helps the reforming process while imposing an energy penalty during sorbent regeneration, as illustrated in Fig. 10. Furthermore, adding excess sorbent has minimal impact on improving CO_2 capture, as previously explained. The marginal gains in CO_2 release do not justify the significant energy penalty for regenerating the extra sorbent. Therefore, optimisation is required to find the sorbent circulation rate that balances adequate CO_2 capture with sustainable thermal management and energy usage, rather than increasing sorbent inventory.

The temperature drop profiles across the reformer and calciner units, shown in Fig. 10, provide insight into how sorbent loading impacts heat transfer. In the reformer, cases with relatively large sorbent amounts (C-S=0.3 and 1.3) demonstrated lower temperature drop with time, compared to the case having a lower sorbent loading (C-S=3). The low temperature drop suggests that higher sorbent loadings aided in maintaining heat within the reformer/carbonator via exothermic carbonation reaction. Conversely, the temperature drop in the calciner followed the opposing pattern, as seen in Fig. 10b. The scenario with the highest sorbent loading (C-S=0.3) exhibited the greatest temperature drop, followed by intermediate (C-S=1.3) and then lowest (C-S=3) sorbent conditions. This suggests a larger heat sink was imposed on the calciner by higher sorbent mass, making more heat to be absorbed via the solid phase. Additionally, the relatively low temperature drop observed in C-S=3 (low sorbent loading) is also associated with the low spent sorbent being sent to the calciner. These results indicate that the bed temperature profiles in the calciner are sensitive to variations in sorbent loading. Therefore, careful thermal management, through improved heat integration to the calciner, will be necessary to maintain sufficient temperature for complete regeneration as loading increases.

To shed more light on the thermal behaviour of the reactor beds, it will be informative to examine the temperature distribution profiles within the reactors. Fig. 11 and Fig. 12 show the contour plots of the modelled temperature distributions for CFB1 and CFB2, respectively, taken at the centre of the reformer and calciner reactor beds at different sorbent loadings and simulation times. In the reformer, the higher sorbent cases (C-S 0.3, 1.3) maintain a more uniform temperature contour with less radial variation compared to the lower sorbent case (C-S 3), particularly as the reaction and circulation progresses. The lower sorbent case (C-S 3) takes more time to achieve uniformity especially in CFB 1. Similar observation is seen in the calciners where the higher sorbent cases (C-S 0.3, 1.3) achieve uniformity as time progresses but reducing in temperature, while C-S 3 takes more time to reach a uniform temperature distribution.

3.4. Hydrodynamic behaviour within the reactors

Fluidisation hydrodynamics impact on reactor performance factors such as gas-solids contacting, mass and heat transfer, and reaction kinetics [71]. The hydrodynamic characteristics of the two bubbling

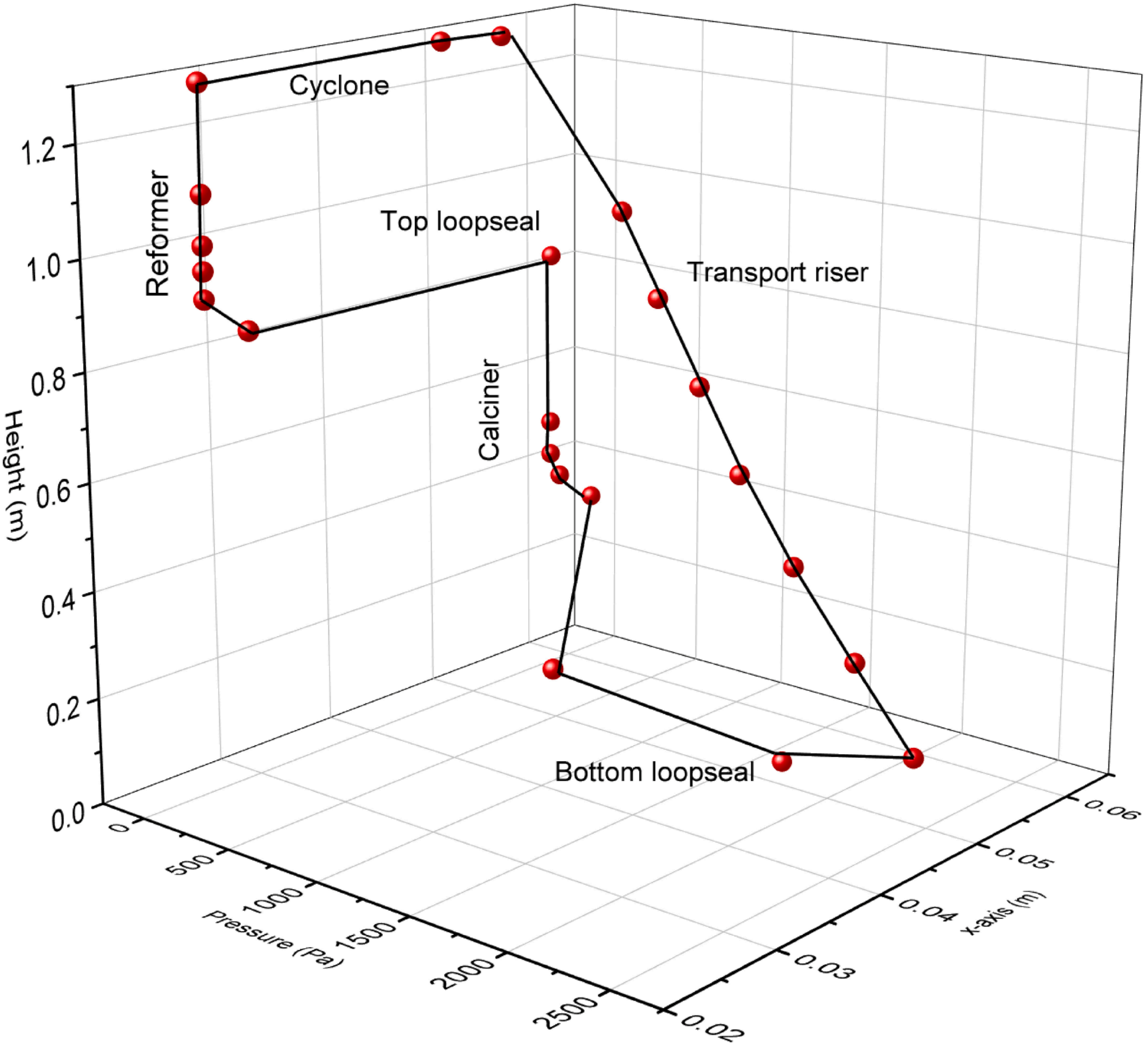

Fig. 13. Time-averaged pressure distribution profile along the heights of the reformer/carbonator, top loopseal, calciner, bottom loopseal, transport riser and cyclone for CFB1.

fluidised bed reactors, CFB1 and CFB2, were evaluated at C-S (=1.3) and compared through analysis of pressure profiles, particle volume fraction and solids distribution. This section will discuss these hydrodynamic studies and examine how the geometrical configuration of each reactor influences flow characteristics.

3.4.1. *Pressure profiles*

Pressure distribution provides insights into solids holdup, mixing, and transport dynamics [72]. Fig. 13 and Fig. 14 display the full-loop pressure profile along the heights of the CFB systems, CFB1 and CFB2. Data points were placed at various heights along the centreline of the reformer/carbonators, calciners, top and bottom loopseals and the transport risers. For both designs, there is a gradual decrease in pressure along the length of the transport riser section as solids are transported upward. The pressure drop remains relatively small across the connections feeding into the cyclone units. Within the cyclones and upper sections of the reformer/carbonator reactors, the pressure levels off at a near-constant value. However, a slight increase is observed lower down in the reactors where the solids holdup begins to build up again. A similar minor increase in pressure also occurs at the top loopseal as solids transfer to the calciner. This was followed by a constant reduction and then slight increase again at the calciner inlet and outlet, respectively. Finally, a sharp spike in pressure is noted within the base of the bottom loopseal, indicating high level of solids accumulation. The high pressure profile in the loopseal region is especially important for maintaining proper solids circulation in such a dual circulating fluidised bed system [73,74].

The maximum simulated pressure drops across key components of the dual fluidised bed systems (the reactors, loopseals and transport riser) are summarised in Table 10. These maximum values were extracted from the CPFD-generated pressure profiles at the bottom region of each reactor, loop seal, and riser where the highest pressures occurred. Generally, the pressure drops across the reformer and top loopseals connecting to the calciner tend to be lower in magnitude

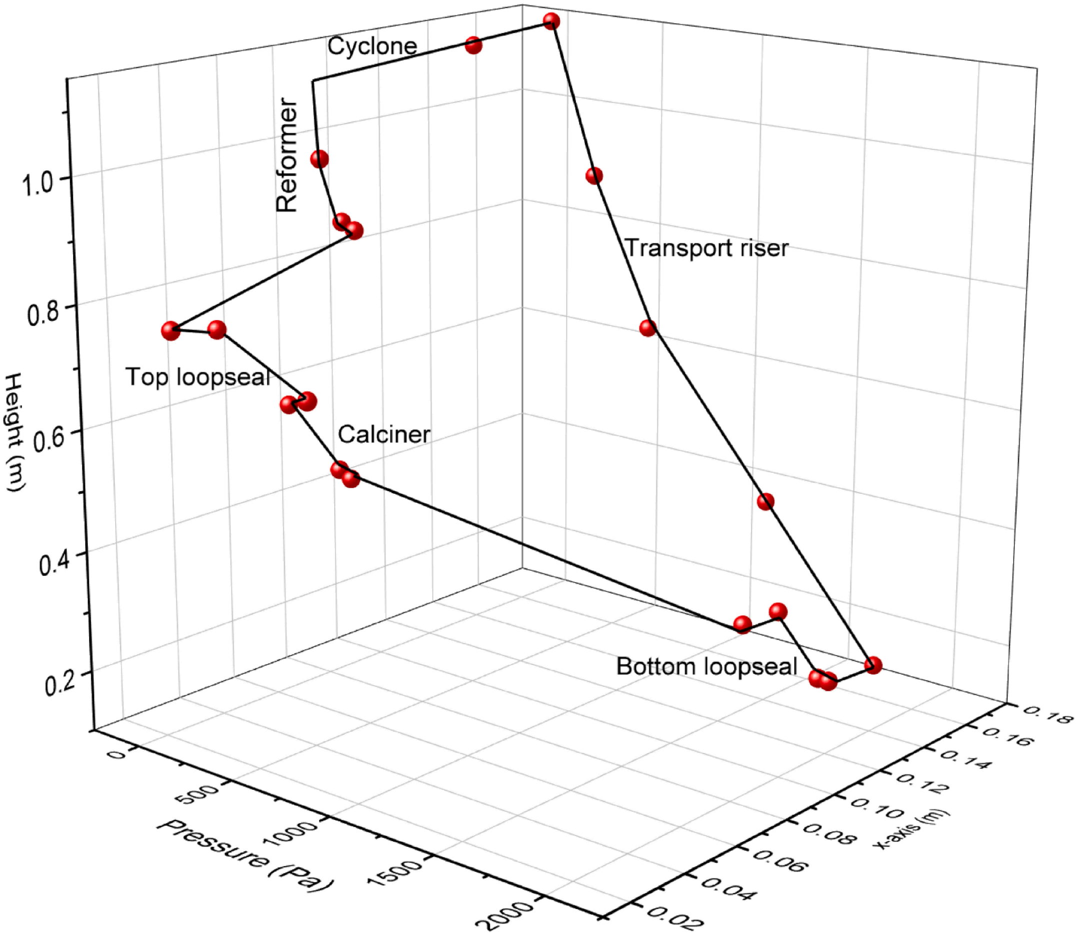

Fig. 14. Time-averaged pressure distribution profile along the heights of the reformer/carbonator, top loopseal, calciner, bottom loopseal, transport riser and cyclone for CFB2.

Table 10
Maximum pressure drops across the key components of the system for CFB1 and CFB2.

Maximum pressure drop	CFB1 (Pa)	CFB2 (Pa)
Reformer/carbonator	251.52	245.89
Top loopseal	780.06	658.02
Calciner	300.67	326.56
Bottom loopseal	2175	1982.12
Transport riser	2135.60	1942.80

compared to those in the calciner reactor and associated bottom loopseals, with the highest simulated pressure in the system occurring in the bottom loopseal. This is due to large solid holdup and high resistance to solids flowrate in the opening between the supply pipe (connected to the calciner) and the recycle pipe (connected to the riser) [75]. Meanwhile, the high pressure drops occurring within the transport riser zones is consistent with the high velocities and circulation rates required to transport particles over long characteristic paths [76].

CFB1 exhibited a notably higher overall pressure drop compared to CFB2 under similar operating conditions. The percent difference in simulated total pressure drop between the two systems ranged from 2.20 % to 15.60 %. The largest deviation was observed in the top loopseal, where the total pressure drop for CFB1 was 15.60 % higher than CFB2. The relatively high simulated pressure drops in CFB1 signify greater flow resistance compared to CFB2.

3.4.2. Particle volume fraction

Fig. 15 displays the radially distributed, time-averaged particle volume fraction profiles extracted from the simulations at the central bed height ($1.87 < H_B < 2$ cm) of both reactors – CFB1 and CFB2. The profiles tend to be slightly higher near the wall than at the centre, especially for CFB2. The gradual drop and peaks near the walls for each bed indicate high concentrations of solids at the walls as bubbles travel upwards through the central region. As gas bubbles rise through the centre of the bed, they exert forces on surrounding particles and push solids nearby in the radial direction toward the wall, while propelling particles ahead in the axial flow direction [77]. However, the particle fraction distribution in the reformer shows a slightly different trend near the walls, particularly for CFB1. Since they both have the same fluidising gas, this difference in profiles between CFB1 and CFB2 reformers is likely caused by geometric factors. In CFB1, a lower particle volume fraction is observed near the wall compared to the central region, as shown in Fig. 15 for normalised diameters under 0.3. This reversed wall effect indicates bubbles are concentrating more towards the reactor periphery rather than the core. This altered bubble flow is likely caused by the internal overflow pipe in CFB1′s reformer being positioned close to the wall. The pipe obstruction may block lateral movement of bubbles, forcing them to travel upwards closer to the wall and displacing more particles inward. Nevertheless, the profiles appear fairly uniform across the radius for both systems, indicative of effective radial mixing by bed bubbles.

3.4.3. Solids distribution

The fluidised bed reactors contain a mixture of CaO sorbent, catalytic particles, and $CaCO_3$ product. Analysing the distinct concentration

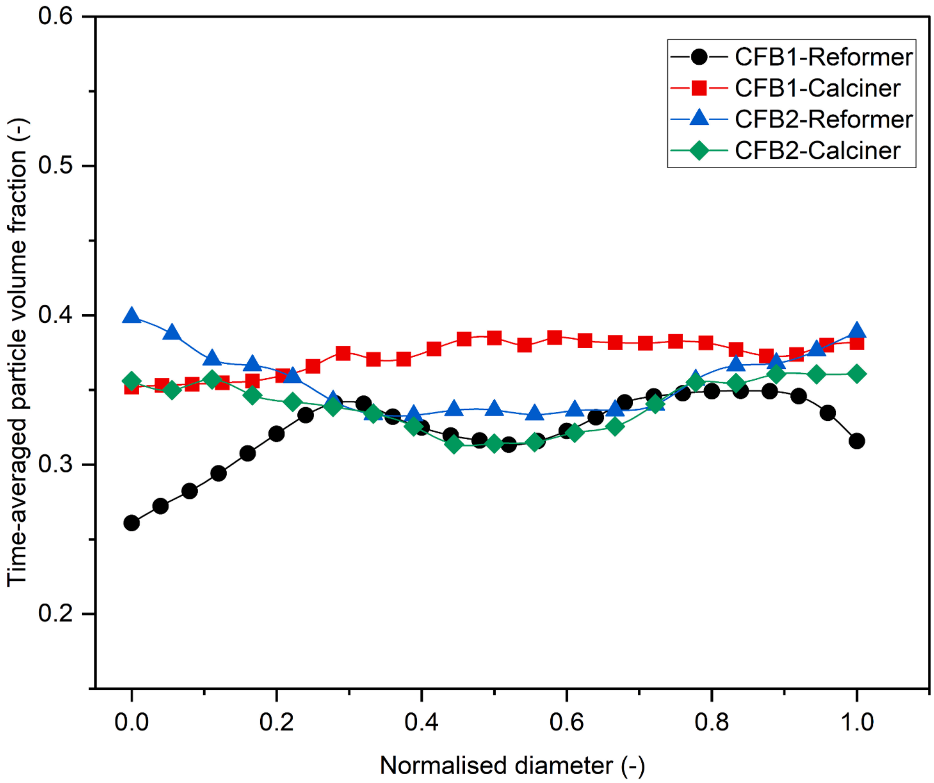

Fig. 15. Radial distribution of time-averaged particle volume fraction at the central bed heights of the reformer and calciner for CFB1 and CFB2.

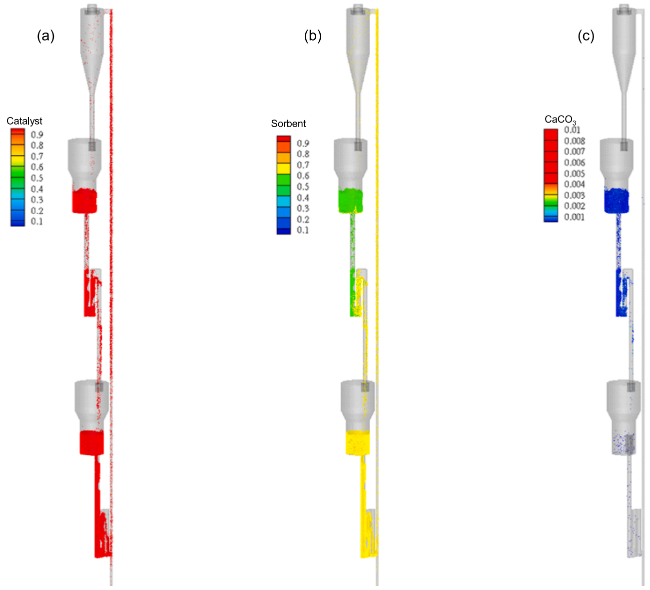

Fig. 16. Distribution of (a) catalyst, (b) sorbent and (c) $CaCO_3$ within the full-loop system for CFB1 coloured by mass fraction.

profiles for these solids can reveal segregation patterns and mixing behaviour. Therefore, the distribution of the solids' species are presented in Fig. 16 and Fig. 17 to give further perspectives on the distribution of the sorbent, catalyst, and $CaCO_3$ product particles in the full-loop system. It is important to note that the catalyst mass fraction is normalised based on its pure fraction in the total reactor inventory, and hence remains around a value of 1 throughout. Meanwhile, the CaO sorbent mass fraction is normalised by the total sorbent (CaO.MgO) concentration circulated in the system. The $CaCO_3$ product fraction depends directly on the local availability of CaO particles and is also normalised based on the total sorbent. Examining the contours after 200 s of simulated operation first reveals the expected result that CaO mass fraction is lower in the reformers versus calciners for both CFB1 and CFB2. However, CFB2 demonstrates notably higher $CaCO_3$ levels in the reformer and slightly in the calciner, suggesting improved sorbent utilisation. Nonetheless, no apparent segregation of solids was observed for CFB1 and CFB2 upon further analysis of solids distribution and solids were uniformly distributed.

4. Conclusions

This study investigated the impact of various catalyst-to-sorbent (C-S) ratios and two bed designs on the chemical performance of a dual circulating fluidised bed system for SE-SR of methane. Properties including product composition, thermal performance and solids distribution, were compared between the two bed geometry designs. Three C-S mass ratios (0.3, 1.3 and 3) were explored to analyse SE-SR's chemical behaviour and hydrodynamic characteristics in a CFB system. At a low C-S of 0.3, methane conversion was lowest with a product gas relatively high in unconverted CH_4 and CO, and low in H_2, suggesting incomplete reforming and CO shift reactions due to insufficient catalyst contact time. As a result, CO_2 capture was negatively impacted due to lower CO_2 partial pressures and driving force. A moderate C-S of 1.3 resulted in improved methane conversion and reduced levels of CO and CO_2 in the product, with the highest H_2 yield. At C-S=3, methane conversion decreased relative to the baseline C-S=1.3, and CO_2 emissions was the highest. However, the negative effects caused by low catalytic activity exceeded those caused by low sorbent activity on the overall process performance. Within the parameters of this study, catalyst activity has a more pronounced effect on methane conversion efficiency, hydrogen yield, and process efficiency than on carbon capture efficiency, while low sorbent loading impacts carbon capture efficiency and has relatively less influence on methane conversion, process efficiency, and hydrogen yield.

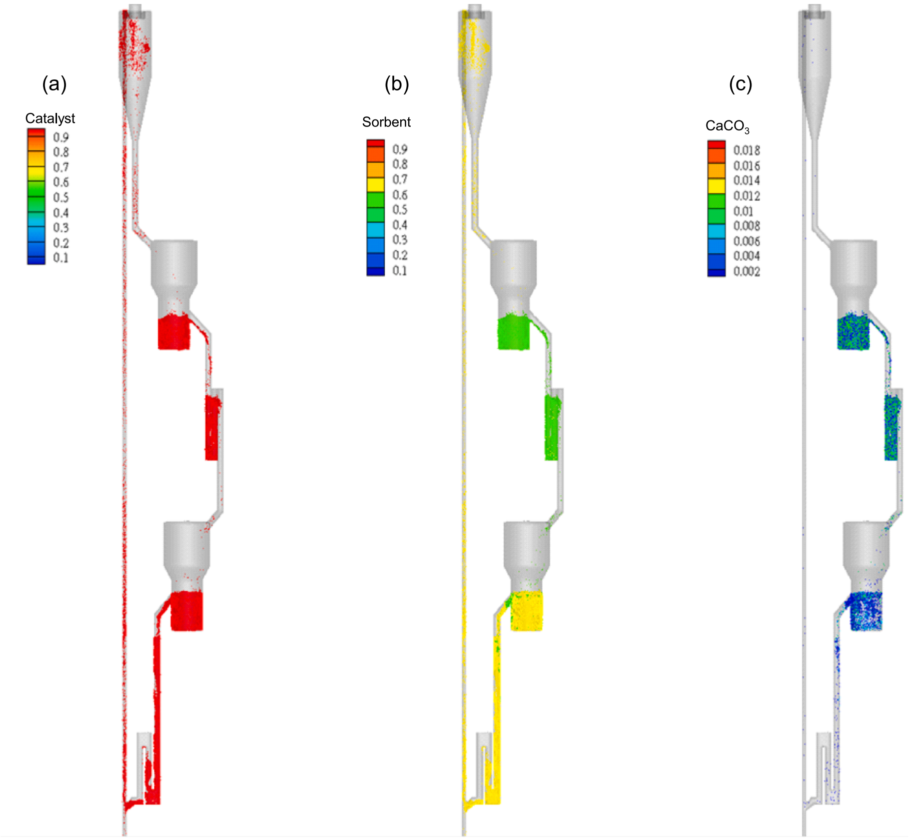

Fig. 17. Distribution of (a) catalyst, (b) sorbent and (c) $CaCO_3$ within the full-loop system for CFB2 coloured by mass fraction.

The C-S ratio also influenced heat management in the system. While higher sorbent loading (C-S=0.3) enhanced heat retention in the reformer, it risked a steeper temperature drop in the calciner, which will inadvertently increase regeneration energy penalties. For optimal process efficiency, adjusting solid circulation rates, together with sorbent inventory, can help alleviate energy penalties associated with calcination temperature drop. The use of bifunctional catalysts may also enhance sorption kinetics at lower mass loadings, reducing heat requirements in the calciner. The instantaneous temperature contours revealed that achieving quick temperature homogenisation proved challenging at very low catalyst or sorbent levels.

The solids volume fraction profiles provided insights into bubble flow patterns within the two bed designs. In CFB1, bubbles appeared to preferentially migrate towards the wall perimeter, as indicated by the downward trend in particle concentration moving radially outward. Meanwhile, CFB2 exhibited a more gently downward sloped profile at the centre, suggesting a tendency for bubbles to accumulate more towards the central axis rather than the perimeter. Solids concentration contours revealed the expected reduced CaO fraction in reformers against the calciners, validating the cyclic carbonation-calcination process. A uniform $CaCO_3$ distribution were seen in the reformers indicating adequate contact between phases without noticeable particle segregation. Whilst the study utilised only two reactor designs, the results indicated that further increase in reactor design complexity (as seen in CFB1) did not significantly boost performance beyond the basic design (CFB2). However, testing a wider range of reactor bed designs could help validate this finding.

Beyond the effort to model SE-SR of methane in circulating fluidised beds, the CPFD modelling approach adopted in this study also allows for the simulation of highly dense solid conditions, which is characteristic of industrial-scale reactors. This makes the model well-suited for investigations spanning lab to commercial implementation of SE-SR. Additionally, maintaining an optimal C-S solid ratio will be important at large scale, as this study has revealed that any imbalance can compromise thermal control – a challenging aspect in industrial facilities.

It is important to highlight that one limitation of this research is that the model used simple assumptions that did not fully capture the complexities of industrial systems by excluding submodels for catalyst deactivation and sorbent performance decline over multiple cycles. The next steps should involve long periods of experimental testing to predict long-term cyclic performance. Under this condition, combined data on performance changes over catalyst lifetimes and sorption-regeneration cycles can be generated. This data could then be used to develop advanced kinetic submodels that describe SE-SR performance decline during continuous operations.

CRediT authorship contribution statement

Chinonyelum Udemu: Conceptualization, Formal analysis, Methodology, Software, Validation, Visualization, Writing – original draft, Writing – review & editing. **Carolina Font-Palma:** Writing – review & editing, Supervision, Methodology, Funding acquisition, Conceptualization.

Declaration of competing interest

The authors declare that they have no known competing financial interests or personal relationships that could have appeared to influence the work reported in this paper.

Data availability

Data will be made available on request.

Acknowledgments

This work was supported by funding from Net Zero Research (formerly BF2RA), UK and the Petroleum Technology Development Fund (PTDF), Nigeria. The authors are also grateful to Dr. Bjørnar Arstad at SINTEF, Norway, for providing the data used in this study, and to EDF Energy, UK and CPFD Software, LLC for their invaluable technical support. Authors also acknowledge the support from the University of Hull, UK's VIPER (the High Performance Computing cluster) team, and the Higher Education Innovation Funding (HEIF) 2021/22.

References

[1] Sazali N. Emerging technologies by hydrogen: A review. Int J Hydrogen Energy 2020;45:18753–71. https://doi.org/10.1016/j.ijhydene.2020.05.021.
[2] Udemu C, Font-Palma C. Potential cost savings of large-scale blue hydrogen production via sorption-enhanced steam reforming process. Energy Convers Manag 2024;302:118132. https://doi.org/10.1016/j.enconman.2024.118132.
[3] Cherbański R, Molga E. Sorption-enhanced steam-methane reforming with simultaneous sequestration of CO_2 on fly ashes – Proof of concept and simulations for gas-solid-solid trickle flow reactor. Chem Eng Process 2018;124:37–49. https://doi.org/10.1016/j.cep.2017.11.010.
[4] Obradović A, Levec J. High purity hydrogen with sorption-enhanced steam methane reforming in a gas-solid trickle bed reactor. Ind Eng Chem Res 2017;56:13301–9. https://doi.org/10.1021/acs.iecr.7b01832.
[5] Ramachandran PA, Dudukovi MP, Mills PL. Recent advances in the analysis and design of trickle-bed reactors. vol. 10. 1987.
[6] Ranade V, Chaudhari R, Gunjal PR. Trickle Bed Reactors. Elsevier 2011. https://doi.org/10.1016/C2009-0-16553-4.
[7] Li ZS, Cai NS. Modeling of multiple cycles for sorption-enhanced steam methane reforming and sorbent regeneration in fixed bed reactor. Energy Fuel 2007;21:2909–18. https://doi.org/10.1021/ef070112c.
[8] Diglio G, Hanak DP, Bareschino P, Pepe F, Montagnaro F, Manovic V. Modelling of sorption-enhanced steam methane reforming in a fixed bed reactor network integrated with fuel cell. Appl Energy 2018;210:1–15. https://doi.org/10.1016/j.apenergy.2017.10.101.
[9] Fernández J, Abanades J. Overview of the Ca–Cu looping process for hydrogen production and/or power generation. Curr Opin Chem Eng 2017;17:1–8. https://doi.org/10.1016/j.coche.2017.04.010.
[10] Meyer J, Mastin J, Smeets R. Hydrogen Production from Biogas by Sorption-Enhanced Steam Methane Reforming (SE-SMR) Demonstration of the Novel Process at the HyNor Lillestrøm Hydrogen Station. 2011.
[11] Johnsen K, Grace JR, Elnashaie SSEH, Kolbeinsen L, Eriksen D. Modeling of sorption-enhanced steam reforming in a dual fluidized bubbling bed reactor. Ind Eng Chem Res 2006;45:4133–44. https://doi.org/10.1021/ie0511736.
[12] Wang J, Wang Y, Jakobsen HA. The modeling of circulating fluidized bed reactors for SE-SMR process and sorbent regeneration. Chem Eng Sci 2014;108:57–65. https://doi.org/10.1016/j.ces.2013.12.012.
[13] Phuakpunk K, Chalermsinsuwan B, Putivisutisak S, Assabumrungrat S. Simulations of sorbent regeneration in a circulating fluidized bed system for sorption enhanced steam reforming with dolomite. Particuology 2020;50:156–72. https://doi.org/10.1016/j.partic.2019.08.005.
[14] Di NA, Calchetti G, Di CA, Stendardo S. Sorption enhanced steam methane reforming in a bubbling fluidized bed reactor: Simulation and analysis by the CPFD method. Comput Chem Eng 2023;169:108080. https://doi.org/10.1016/j.compchemeng.2022.108080.
[15] Sánchez RA, Chao Z, Solsvik J, Jakobsen HA. An investigation of the heat integration between the two riser units constituting a circulating fluidized bed reactor for the SE-SMR process. Energy Procedia, vol. 37, Elsevier Ltd; 2013, p. 1218–27. Doi: 10.1016/j.egypro.2013.05.220.
[16] Jakobsen JP, Halmøy E. Reactor modeling of sorption enhanced steam methane reforming. Energy Procedia 2009;1:725–32. https://doi.org/10.1016/j.egypro.2009.01.096.
[17] Bello MM, Abdul Raman AA, Purushothaman M. Applications of fluidized bed reactors in wastewater treatment – A review of the major design and operational parameters. J Clean Prod 2017;141:1492–514. https://doi.org/10.1016/j.jclepro.2016.09.148.
[18] Cheng Y, Wei F, Yang G, Jin Y. Inlet and outlet effects on flow patterns in gas-solid risers. Powder Technol 1998;98:151–6. https://doi.org/10.1016/S0032-5910(98)00030-8.
[19] Lopes GC, Rosa LM, Mori M, Nunhez JR, Martignoni WP. CFD Study of Industrial FCC Risers: The Effect of Outlet Configurations on Hydrodynamics and Reactions. Int J Chem Eng 2012;2012:1–16. https://doi.org/10.1155/2012/193639.
[20] Gómez-Velásquez N, López-Montoya T, Bustamante-Chaverra CA, Nieto-Londoño C. Parametric study of particles homogenization in cold-flow riser reactors. Int J Thermofluids 2021;9:100058. https://doi.org/10.1016/j.ijft.2020.100058.
[21] Udemu C, Font-Palma C. Modelling of sorption-enhanced steam reforming (SE-SR) process in fluidised bed reactors for low-carbon hydrogen production: A review. Fuel 2023;340:127588. https://doi.org/10.1016/J.FUEL.2023.127588.
[22] Loha C, Chattopadhyay H, Chatterjee PK. Three dimensional kinetic modeling of fluidized bed biomass gasification. Chem Eng Sci 2014;109:53–64. https://doi.org/10.1016/J.CES.2014.01.017.
[23] Kraft S, Kuba M, Kirnbauer F, Bosch K, Hofbauer H. Optimization of a 50 MW bubbling fluidized bed biomass combustion chamber by means of computational particle fluid dynamics. Biomass Bioenergy 2016;89:31–9. https://doi.org/10.1016/J.BIOMBIOE.2016.02.020.
[24] Arstad B, Blom R, Bakken E, Dahl I, Jakobsen JP, Røkke P. Sorption-enhanced methane steam reforming in a circulating fluidized bed reactor system. Energy Procedia 2009;1:715–20. https://doi.org/10.1016/j.egypro.2009.01.094.
[25] CPFD Software LLC. Barracuda Virtual Reactor® User Manual 2023.
[26] Andrews MJ, O'Rourke PJ. The multiphase particle-in-cell (MP-PIC) method for dense particulate flows. Int J Multiph Flow 1996;22:379–402. https://doi.org/10.1016/0301-9322(95)00072-0.
[27] Snider DM. An incompressible three-dimensional multiphase particle-in-cell model for dense particle flows. J Comput Phys 2001;170:523–49. https://doi.org/10.1006/JCPH.2001.6747.
[28] Wang S, Yang X, Xu S, Zhang K, Li B. Evaluation of sorption-enhanced reforming of biodiesel by-product in fluidized beds by means of CFD approach. Fuel 2018;214:115–22. https://doi.org/10.1016/J.FUEL.2017.10.128.
[29] Di Nardo A, Savuto E, Calchetti G, Stendardo S. Computational particle fluid dynamics 3D simulation of the sorption-enhanced steam methane reforming process in a dual fluidized bed of bifunctional sorbent-catalyst particles. Powder Technol 2023;424:118568. https://doi.org/10.1016/j.powtec.2023.118568.
[30] Wang S, Xu S, Liu S, Hu B. Prediction of sorption-enhanced reforming process on hydrotalcite sorbent in a fluidized bed reactor. Energy Convers Manag 2019;180:924–30.
[31] Gao X, Li T, Sarkar A, Lu L, Rogers WA. Development and validation of an enhanced filtered drag model for simulating gas-solid fluidization of Geldart A particles in all flow regimes. Chem Eng Sci 2018;184:33–51. https://doi.org/10.1016/j.ces.2018.03.038.
[32] Yang N, Wang W, Ge W, Wang L, Li J. Simulation of heterogeneous structure in a circulating fluidized-bed riser by combining the two-fluid model with the EMMS approach. Ind Eng Chem Res 2004;43:5548–61. https://doi.org/10.1021/IE049773C/ASSET/IMAGES/LARGE/IE049773CF00013.JPEG.
[33] Li J, Kwauk M. Particle-fluid two-phase flow: the energy-minimization multi-scale method. Metall Indust Press 1994.
[34] Yang WC. Handbook of Fluidization and Fluid-Particle Systems. Taylor & Francis 2003.
[35] Fan LS, Zhu C. Principles of Gas-Solid Flows. Cambridge University Press; 1998.
[36] Numaguchi T, Kikuchi K. Intrinsic kinetics and design simulation in a complex reaction network; steam-methane reforming. Tenth Int Symposium Chem Reaction Eng 1988:2295–301. https://doi.org/10.1016/B978-0-08-036969-3.50086-5.
[37] Xu J, Froment GF. Methane steam reforming, methanation and water-gas shift: I. Intrinsic kinetics AIChE J 1989;35:88–96. https://doi.org/10.1002/aic.690350109.
[38] Quirino PPS, Amaral A, Pontes KV, Rossi F, Manenti F. Impact of kinetic models in the prediction accuracy of an industrial steam methane reforming unit. Comput Chem Eng 2021;152:107379. https://doi.org/10.1016/J.COMPCHEMENG.2021.107379.
[39] Hou K, Hughes R. The kinetics of methane steam reforming over a Ni/-Al 2 O catalyst. vol. 82. 2001.
[40] Sun P, Grace JR, Lim CJ, Anthony EJ. Determination of intrinsic rate constants of the CaO-CO_2 reaction. Chem Eng Sci 2008;63:47–56. https://doi.org/10.1016/j.ces.2007.08.055.
[41] Abanades JC, Alvarez D. Conversion limits in the reaction of CO_2 with Lime. Energy Fuel 2003;17:308–15. https://doi.org/10.1021/ef020152a.
[42] Abanades JC, Anthony EJ, Lu DY, Salvador C, Alvarez D. Capture of CO_2 from combustion gases in a fluidized bed of CaO. AIChE J 2004;50:1614–22. https://doi.org/10.1002/AIC.10132.
[43] Fedunik-Hofman L, Bayon A, Donne SW. Kinetics of solid-gas reactions and their application to carbonate looping systems. Energies (Basel) 2019:12. https://doi.org/10.3390/en12152981.
[44] García-Labiano F, Abad A, de Diego LF, Gayán P, Adánez J. Calcination of calcium-based sorbents at pressure in a broad range of CO_2 concentrations. Chem Eng Sci 2002;57:2381–93. https://doi.org/10.1016/S0009-2509(02)00137-9.
[45] Kanellis G, Zeneli M, Nikolopoulos N, Hofmann C, Ströhle J, Karellas S, et al. CFD modelling of an indirectly heated calciner reactor, utilized for CO_2 capture, in an Eulerian framework. Fuel 2023;346:128251. https://doi.org/10.1016/j.fuel.2023.128251.
[46] Barin I, Platzki G. Thermochemical data of pure substances. vol. 304. Wiley Online Library; 1989.
[47] O'Rourke PJ, Snider DM. A new blended acceleration model for the particle contact forces induced by an interstitial fluid in dense particle/fluid flows. Powder Technol 2014;256:39–51. https://doi.org/10.1016/j.powtec.2014.01.084.
[48] LeVeque RJ. Finite volume methods for hyperbolic problems. vol. 31. Cambridge university press; 2002.
[49] Shakor ZM, Al-Shafei EN. The mathematical catalyst deactivation models: a mini review. RSC Adv 2023;13:22579–92. https://doi.org/10.1039/D3RA02912C.
[50] Arstad B, Prostak J, Blom R. Continuous hydrogen production by sorption enhanced steam methane reforming (SE-SMR) in a circulating fluidized bed reactor: Sorbent to catalyst ratio dependencies. Chem Eng J 2012;189–190:413–21.
[51] Wang S, Luo K, Hu C, Lin J, Fan J. CFD-DEM simulation of heat transfer in fluidized beds: Model verification, validation, and application. Chem Eng Sci 2019;197:280–95. https://doi.org/10.1016/j.ces.2018.12.031.

[52] Soomro M, Hughes R. The thermal conductivity of porous catalyst pellets. Can J Chem Eng 1979;57:24–8. https://doi.org/10.1002/cjce.5450570104.

[53] Khan KA, Khan SZ, Khan MA. Effective thermal conductivity of two-phase composites containing highly conductive inclusions. J Reinf Plast Compos 2016;35:1586–99. https://doi.org/10.1177/0731684416661044.

[54] Mortazavi B, Shojaei F, Rabczuk T, Zhuang X. High tensile strength and thermal conductivity in BeO monolayer: A first-principles study. FlatChem 2021;28:100257. https://doi.org/10.1016/j.flatc.2021.100257.

[55] Aloisi I, Jand N, Stendardo S, Foscolo PU. Hydrogen by sorption enhanced methane reforming: A grain model to study the behavior of bi-functional sorbent-catalyst particles. Chem Eng Sci 2016;149:22–34. https://doi.org/10.1016/j.ces.2016.03.042.

[56] Aspen Technology Inc. Aspen Plus® 2022.

[57] Chanburanasiri N, Ribeiro AM, Rodrigues AE, Arpornwichanop A, Laosiripojana N, Praserthdam P, et al. Hydrogen production via sorption enhanced steam methane reforming process using Ni/CaO multifunctional catalyst. Ind Eng Chem Res 2011;50:13662–71. https://doi.org/10.1021/ie201226j.

[58] Hwang K-R, Lee C-B, Park J-S. Advanced nickel metal catalyst for water–gas shift reaction. J Power Sources 2011;196:1349–52. https://doi.org/10.1016/j.jpowsour.2010.08.084.

[59] Cunha AF, Moreira MN, Mafalda Ribeiro A, Ferreira AP, Loureiro JM, Rodrigues AE. How to overcome the water–gas-shift equilibrium using a conventional nickel reformer catalyst. Energ Technol 2015;3:1205–16. https://doi.org/10.1002/ente.201500175.

[60] Hu Y, Cui H, Cheng Z, Zhou Z. Sorption-enhanced water gas shift reaction by in situ CO_2 capture on an alkali metal salt-promoted $MgO-CaCO_3$ sorbent. Chem Eng J 2019;377:119823. https://doi.org/10.1016/j.cej.2018.08.209.

[61] Chen H, Zhao C, Li Y, Chen X. CO_2 Capture performance of calcium-based sorbents in a pressurized carbonation/calcination loop. Energy Fuel 2010;24:5751–6. https://doi.org/10.1021/ef100565d.

[62] Radfarnia HR, Iliuta MC. Hydrogen production by sorption-enhanced steam methane reforming process using CaO-Zr/Ni bifunctional sorbent–catalyst. Chem Eng Process 2014;86:96–103. https://doi.org/10.1016/j.cep.2014.10.014.

[63] Kazi SS, Aranda A, Meyer J, Mastin J. High performance CaO-based sorbents for pre- and post- combustion CO_2 capture at high temperature. Energy Procedia 2014;63:2207–15. https://doi.org/10.1016/j.egypro.2014.11.240.

[64] Di Giuliano A, Gallucci K, Kazi SS, Giancaterino F, Di Carlo A, Courson C, et al. Development of Ni- and CaO-based mono- and bi-functional catalyst and sorbent materials for sorption enhanced steam methane reforming: performance over 200 cycles and attrition tests. Fuel Process Technol 2019;195:106160. https://doi.org/10.1016/j.fuproc.2019.106160.

[65] Pistonesi C, Juan A, Irigoyen B, Amadeo N. Theoretical and experimental study of methane steam reforming reactions over nickel catalyst. Appl Surf Sci 2007;253:4427–37. https://doi.org/10.1016/j.apsusc.2006.09.054.

[66] Jokar SM, Parvasi P, Basile A. The performance evaluation of an industrial membrane reformer with catalyst-deactivation for a domestic methanol production plant. Int J Hydrogen Energy 2019;44:25730–9. https://doi.org/10.1016/j.ijhydene.2019.08.062.

[67] Gorji-Kandi S, Alavi-Amleshi SM, Mostoufi N. Experimental investigating the effect of bed geometry on solids mixing in fluidized beds. Part Sci Technol 2016;34:127–33. https://doi.org/10.1080/02726351.2015.1054532.

[68] Di CA, Bocci E, Zuccari F, Dell'era A. Numerical investigation of sorption enhanced steam methane reforming process using computational fluid dynamics Eulerian-Eulerian code. Ind Eng Chem Res 2010;49:1561–76. https://doi.org/10.1021/ie900748t.

[69] Herce C, Cortés C, Stendardo S. Computationally efficient CFD model for scale-up of bubbling fluidized bed reactors applied to sorption-enhanced steam methane reforming. Fuel Process Technol 2017;167:747–61. https://doi.org/10.1016/j.fuproc.2017.07.003.

[70] Herce C, Cortés C, Stendardo S. Numerical simulation of a bubbling fluidized bed reactor for sorption-enhanced steam methane reforming under industrially relevant conditions: Effect of sorbent (dolomite and CaO-Ca12Al14O33) and operational parameters. Fuel Process Technol 2019;186:137–48. https://doi.org/10.1016/j.fuproc.2019.01.003.

[71] Berruti F, Pugsley TS, Godfroy L, Chaouki J, Patience GS. Hydrodynamics of circulating fluidized bed risers: A review. Can J Chem Eng 1995;73:579–602. https://doi.org/10.1002/cjce.5450730502.

[72] Tu Q, Wang H, Ocone R. Application of three-dimensional full-loop CFD simulation in circulating fluidized bed combustion reactors – A review. Powder Technol 2022;399:117181. https://doi.org/10.1016/j.powtec.2022.117181.

[73] Kim SW, Kim SD, Lee DH. Pressure balance model for circulating fluidized beds with a loop-seal. Ind Eng Chem Res 2002;41:4949–56. https://doi.org/10.1021/ie0202571.

[74] Wang Q, Yang H, Wang P, Lu J, Liu Q, Zhang H, et al. Application of CPFD method in the simulation of a circulating fluidized bed with a loop seal Part II—Investigation of solids circulation. Powder Technol 2014;253:822–8. https://doi.org/10.1016/j.powtec.2013.11.040.

[75] Cheng L, Basu P. Effect of pressure on loop seal operation for a pressurized circulating fluidized bed. Powder Technol 1999;103:203–11. https://doi.org/10.1016/S0032-5910(99)00018-2.

[76] Wang X, Liao L, Fan B, Jiang F, Xu X, Wang S, et al. Experimental validation of the gas–solid flow in the CFB riser. Fuel Process Technol 2010;91:927–33. https://doi.org/10.1016/j.fuproc.2010.02.020.

[77] Kunii D, Levenspiel O. Fluidization Engineering 2nd Edition 2013:491.